11 Interspecies Pharmacokinetic Scaling and the Prediction of Human Pharmacokinetics Using Animal and Cell Models

MEIHUA ROSE FENG, NAN ZHENG, XINYUAN ZHANG, YEA MIN HUH, and JING-YU YU
University of Michigan, Ann Arbor, MI, USA

11.1 SUMMARY

Early projection of human pharmacokinetic (PK) properties is of great significance for decision making at several stages in drug discovery and development (e.g., lead compound selection and optimization, first dose in human), and the interspecies allometric scaling is an important tool widely used in the industry for this type of prediction. The allometric scaling is an empirical method that has interested biological and pharmaceutical scientists for more than 100 years. It is developed based on cross-species similarities in anatomy, physiology, and biochemistry with a power function correlating physiological parameters with body size ($Y = aW^b$, where Y is the parameter of interest, W is the body weight, and a and b are the coefficient and exponent of the allometric equation, respectively). The allometric scaling method has been used successfully to describe a number of physiological and anatomical properties and has been applied to the projection of human PK for small-molecule drugs as well as therapeutic proteins. However, for most small-molecule drugs with high cross-species variability in hepatic metabolism, this method may not work well in the extrapolation of hepatic metabolic clearance (CL) from laboratory animals to humans. To improve the predictability of metabolic CL in humans, several modified scaling methods have been recommended and tested. Boxenbaum in 1983 proposed using maximum life span potential (MLP) and brain weight (BRW) as correction factors in allometric scaling since longevity

Encyclopedia of Drug Metabolism and Interactions, 6-Volume Set, First Edition.
Edited by Alexander V. Lyubimov.

is frequently inversely correlated with hepatic cytochrome P450 drug oxidation rates. His work was later supported by the research of other scientists, and their work also demonstrated that the MLP and BRW correction improved the accuracy of human CL prediction when the allometry power exponent b was higher than 0.80—0.90. In 1997, Lave *et al*. integrated the *in vitro* data into the power function by normalizing the *in vivo* CL with *in vitro* metabolic CL and successfully applied their method to human CL prediction of 10 small-molecule drugs that are mainly hepatically eliminated. Nagilla and Ward in 2004 suggested using liver blood flow (LBF) as a correction factor for the scaling of small-molecule drugs. On the basis of their analysis of 103 compounds comparing simple allometry (SA) with LBF or MLP/BRW correction, they concluded that scaling with monkey LBF was the best approach among the methods tested (68% success rate). These modified scaling methods have improved the accuracy of prediction to some extent and are reviewed in this chapter. In recent years, there is an increasing interest in physiologically based pharmacokinetic (PBPK) and cell-based pharmacokinetic (CBPK) modeling. Both approaches are developed based on similar assumption that PK properties could be scaled-up from animals to humans according to fundamental physiological principles. These advanced methods allow the integration of input information from different sources (e.g., physiological and physicochemical properties of a drug molecule, permeability and binding affinity from *in vitro* experiments, PK profiles from animal tests and clinical trials). In addition to the prediction of PK parameters (e.g., CL, volume of distribution), the PBPK and CBPK models could also predict the concentration–time profiles in human blood as well as in tissues associated with efficacy and/or toxicity. The utility of PBPK and CBPK modeling goes beyond the prediction of "first-in-human trial," as it has the potential to be continuously updated with new information (physiological and drug related). Some of the tools and techniques employed in PBPK and CBPK modeling are discussed in the second half of this chapter.

11.2 ALLOMETRIC SCALING

The allometry method was originally developed based on the assumption that mammals generally have similar anatomy, physiology, biochemistry, and cellular structure. This similarity would allow the extrapolation and scaling of physiologic properties (e.g., heart rate, blood flow, blood volume, organ size, longevity) from animals to humans (Fig. 11.1). A power equation $Y = aW^b$ is often used in allometric scaling, where Y is the physiologic variable of interest, W is body weight, and log a and b are the y-intercept and slope obtained from the plot of log Y versus log W, respectively. Animals commonly used in preclinical tests (i.e., mouse, rat, rabbit, monkey, and dog) may not eliminate drugs with the same rate and pathway as humans, and small mammals usually eliminate chemicals faster than large mammals. Since the elimination of many drugs is associated with physiologic properties well described among species (e.g., size and blood flow for the elimination organs), it is assumed that drug elimination may be scaled among mammals, and many successful case studies have been reported in the literature [1–32]. However, the majority of the small-molecule drugs are eliminated via oxidative hepatic metabolism. If there are significant cross-species differences in substrate specificity and/or in enzymes activity, the animal to human extrapolation may

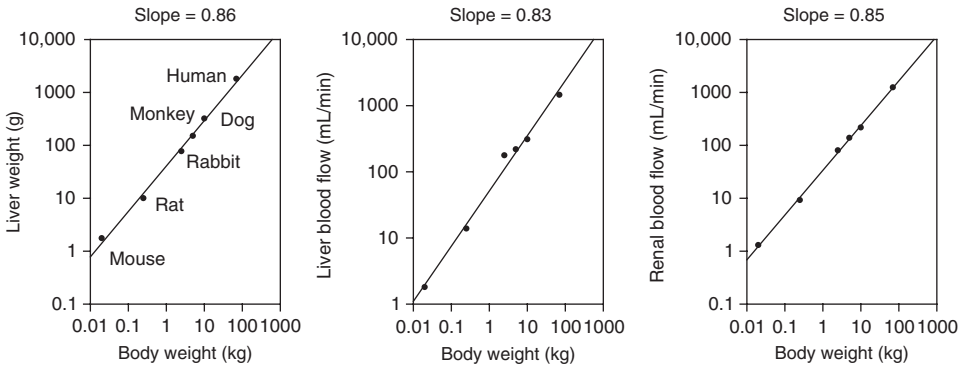

Figure 11.1 Correlation of liver weight, LBF, and renal blood flow versus total body weight in laboratory animals and humans.

fail. To reduce the error in the prediction of metabolic CL in humans, several correction factors have been introduced and are discussed in this section. In recent years, biotechnologically derived peptides and therapeutic proteins have been developed as mainstream therapeutic agents. Peptide and protein drugs (i.e., macromolecule drugs) now constitute a substantial portion of the compounds under preclinical and clinical development in the pharmaceutical industry. The distribution and metabolism of protein-based biotech drugs often follow the mechanisms of endogenous and nutritional proteins with nonspecific proteolysis as a major elimination pathway [33–35]. Owing to their structural similarity as polypeptides, it is generally much easier to predict how peptide and therapeutic proteins will be distributed, metabolized, and eliminated, and they typically have much faster development cycles. As the handling of peptides and proteins is relatively well preserved between different mammalian species, allometric scaling is usually much more successful for macromolecules than for the traditional small-molecule drugs. In this section, the scaling of these two types of drugs is discussed and compared. For some therapeutic proteins, the elimination process is associated with both nonspecific proteolysis and specific receptor-mediated endocytosis and degradation. Owing to the limited number of receptors expressed on the membrane or in the cell, the receptor-mediated degradation process could be saturated at high drug concentrations. For those proteins mainly eliminated with receptor-mediated degradation, saturation of this process would result in an over-proportional increase in systemic exposure, and a decrease of systemic CL with increasing dose (i.e., nonlinear PK). For example, dose-dependent elimination and prolonged half-life at higher doses have been reported for protein drugs erythropoietin, cetuximab, thrombopoietin, and trastuzumab (Herceptin) [36–40]. When this occurs, the systemic CL becomes dose dependent and is generally estimated using the Michaelis–Menten equation. Similar problem may also occur in the scaling of small molecules.

11.2.1 Prediction of Human Clearance Using Single Animal Species with a Fixed Exponent

As mentioned above, a power equation $Y = aW^b$, with Y as the physiologic variable of interest and W as body weight, is generally used in the allometric scaling. When a

log transformation of the power function is performed, the power equation becomes

$$\log(Y) = \log(a) + b \times \log(W)$$

The coefficients a and b can be obtained from a plot of the body weight from several species against the PK parameter of interest on a log–log scale; log (a) is the y-intercept and b is the slope obtained from the plot of $\log(Y)$ versus $\log(W)$. In general, biological frequencies (e.g., heart rate per minute) have an exponent of -0.25, biological time periods (e.g., circulation time, MLP) have an exponent of 0.25, biological rates (e.g., CL, physiological flow rates, and metabolism) have an exponent of 0.75, volume of distribution has an exponent of 1.0, and body surface area has an exponent of 0.67 [2–4,32]. The allometric exponents for most drugs are in a similar range to those from the corresponding biological processes, with exponents of 0.60–0.80 for CL and 0.8–1.0 for volume of distribution (V_d). If the PK data are only available in a single animal species, the CL and V_d in the humans are often estimated using a fixed exponent of 0.75 and 1.0, respectively. The authors have tested the single species (mouse, rat, dog, or monkey) scaling of CL using a fixed b value ranged from 0.60 to 0.85, and the prediction errors from this analysis of 62 small-molecule and 32 macromolecule drugs are presented in Fig. 11.2 and Table 11.1. The results would suggest an optimal value of 0.70–0.80 for the exponent b and to use large animals (e.g., monkey or dog) for single species scaling [41]. In general, the error of human CL prediction is within twofold using monkey PK data and body weight. With the allometry exponent b fixed at 0.70, 0.75, or 0.80, the average error was 1.88-, 1.87-, and 1.86-fold for small-molecule and 1.97-, 1.75-, and 1.61-fold, respectively, for macromolecule drugs. The average error of human CL prediction is higher for the small-molecule drugs using dog as a single species and ranged from 2.4- to 2.9-fold. For macromolecule drugs, the predicted human CL is generally within twofold of the observed value using dog data, with average error ranging from 1.6- to 1.8-fold.

As mentioned previously, LBF is another physiological variable highly correlated to body size and was tested by several groups for its potential application in the extrapolation of hepatic metabolic CL from animals to humans [7,9,10]. The authors have evaluated recently [12] the use of LBF in single species scaling, and the results are summarized in Table 11.2. In general, the method works better for high CL drugs, and the average error of human CL prediction is 1.86- and 1.54-fold using monkey LBF and 2.9- and 2.3-fold using dog LBF for small- and macromolecule drugs, respectively. The average error of human CL prediction is much higher using mouse or rat data (body weight or LBF) for single species scaling [42].

11.2.2 Prediction of Human Clearance Using Two or More Animal Species

In general, allometric scaling is performed using two, three, or more animal species, and many successful case studies have been reported in the literature [1–32]. Conventional allometric scaling often works fairly well in human CL projection when the elimination process is dependent on kidney blood flow or LBF. However, for small-molecule drugs with significant cross-species differences in hepatic metabolism, simple allometric relationships may give poor prediction. Boxenbaum has suggested incorporating MLP into the allometric equation as a correction factor for the scaling of CL ($\text{MLP}\cdot\text{CL} = aW^b$) since longevity is frequently inversely correlated with hepatic

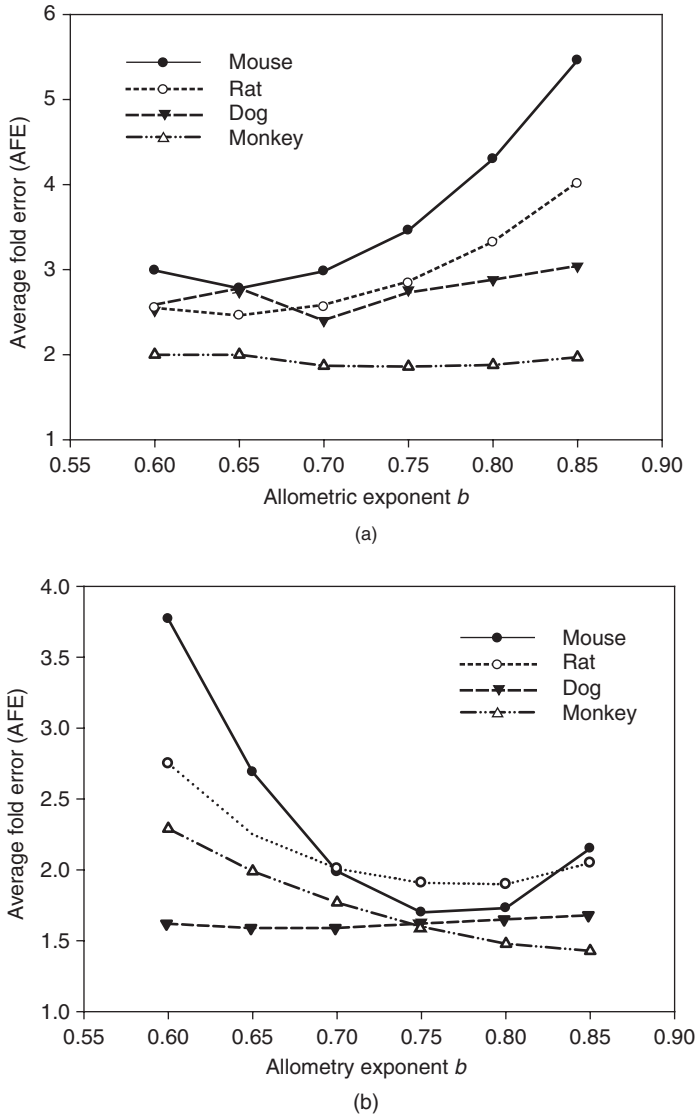

Figure 11.2 Cross-species comparison of the relationship between prediction error [average fold error (AFE)] and allometry exponent b for small-molecule (a) and macromolecule (b) drugs.

cytochrome P450 drug oxidation rates [2,3]. MLP·CL is the total volume from which drug would be cleared per MLP assuming constant drug exposure [2]. With regard to humans, it would appear that the relatively low CL (with respect to liver weight) is paced to their longevity, that is, activity is conserved so as to be extended over a relatively longer chronological MLP. Boxenbaum also explored the possibility of using BRW as a correction factor ($\text{BRW}\cdot\text{CL} = aW^b$) since MLP is closely correlated to BRW [$\text{MLP} = 10.839\cdot(\text{BRW})^{0.636}\cdot(W)^{0.225}$].

Consistent with Boxenbaum's proposal, Feng and others [5–7] also reported that correction with MLP or BRW could help to reduce the error in human CL prediction

TABLE 11.1 Prediction of Human CL Using Single Species Scaling with Fixed Allometry Exponent *b*

		Dog		Monkey	
		Small-Molecule Drug ($N = 60$)	Macromolecule ($N = 10$)	Small-Molecule Drug ($N = 45$)	Macromolecule ($N = 11$)
Average fold error	$b = 0.60$	2.52	1.57	2.0	2.63
	$b = 0.65$	2.74	1.73	2.0	2.28
	$b = 0.70$	2.4	1.75	1.87	1.97
	$b = 0.75$	2.76	1.57	1.86	1.75
	$b = 0.80$	2.88	1.6	1.88	1.61
	$b = 0.85$	3.04	1.63	1.97	1.64

TABLE 11.2 Prediction of Human CL Using Liver Blood Flow (LBF) Scaling Method

	Dog		Monkey	
	Small-Molecule Drug ($N = 60$)	Macromolecule ($N = 10$)	Small-Molecule Drug ($N = 45$)	Macromolecule ($N = 11$)
Average fold error	2.93	2.26	1.86	1.54

[a]This approach predicts human CL according to the following equation: Predicted $CL_{human} = CL_{monkey}$ (LBF_{human}/LBF_{monkey}), where liver blood flow is 21 and 45 mL/min/kg in human and monkey, respectively, as reported in the literature. For a human weighing 70 kg and a monkey weighing 5 kg, the liver blood flow is 1470 and 225 mL/min, respectively.

for small-molecule drugs with SA exponent b higher than 0.85. Examples from Feng's research are presented in Table 11.3. For the seven small-molecule drugs overpredicted using SA ($CL = aW^b$), incorporating BRW into the power equation ($BRW \cdot CL = aW^b$) increased the accuracy of human CL prediction and reduced the average error from 9.13- to 1.82-fold. Additional research from Mahmood [8,13–17] and Tang *et al*. [18] also supported the use of MLP and BRW as correction factors. Mahmood *et al*. and Balian [17] analyzed several series of small-molecule drugs and proposed three approaches for human CL prediction based on the value of the exponent b derived from the power equation $CL = aW^b$. They suggested incorporating MLP into the allometric relationship ($MLP \cdot CL = aW^b$) when the power exponent b is between 0.71 and 1.0 (0.75–0.90 from analysis of nine anticancer drugs) and correcting with BRW ($BRW \cdot CL = aW^b$) when b is higher than 0.90 or 1.0.

On the basis of a similar mechanism, a combined method of SA and multiexponential allometry (MA) was proposed to improve the accuracy of human CL prediction [19]. For the MA approach, human CL was estimated by the equation $CL = aBW^b + cBW^d$, where a and b are the coefficient and slope generated from the SA scaling and c and d are the coefficient and slope for MA. The parameter d is derived based on the slope from the scaling of blood flow rate, organ volume, and organ weight of liver or kidney versus body weight in preclinical species. The slopes of weight, volume, and flow rates of these major excretory organs (liver or kidney) are very similar and approximately

TABLE 11.3 Human CL Prediction with ($CL \cdot BRW = aW^b$) or without ($CL = aW^b$) Brain Weight (BRW) Correction

Drug	Exponent b From SA	Actual Human CL (mol/min/kg)	Predicted/Actual	
			SA	CL × BRW
PD-7	0.97	0.0043	5.6	0.74
PD-8	1.1	8.5	5.7	1.5
Antipyrine	0.93	0.46	11.5	1.8
Theophylline	0.96	0.87	3.6	0.80
Diazepam	1	0.35	32.9	3.8
Valproate	1.16	0.11	9.9	1.9
Midazolam	2.15	11	12.3	2.0
Average fold error			9.13	1.82

equal to 0.9. Therefore, the slope d was fixed as 0.9. The coefficient c was defined as a function of a and b:

$$c = a\left[\frac{\left(1-\frac{3}{2}b\right)}{\left(1-\frac{1}{2}b\right)}\right]$$

As reported by Goteti *et al*. [19], the proposed method helped to reduce the error of human CL prediction for small-molecule drugs with allometry exponent b higher than 0.7. The authors have evaluated the SA + MA method for the human CL prediction of 62 small-molecule drugs and compared with the SA approach with the results presented in Table 11.4. It appears that the SA + MA combination, although still empirical, reduced the average prediction error from 4.2- to 3.1-fold. However, the prediction errors still appear high for these small molecules using the SA + MA approach.

Although the prediction of human CL appears complicated and sometimes problematic for the small-molecule drugs, the SA method generally could predict human CL within twofold for the macromolecule drugs (i.e., therapeutic proteins). The authors have analyzed 32 macromolecule drugs and the outcome is presented in Table 11.4. The average error of human CL prediction is 2.1-fold using the SA, suggesting that the predicted values are normally within twofold of the observed human CL for these protein drugs, probably because the major elimination pathway for these therapeutic proteins is nonspecific proteolysis that is not species-dependent and very different compared to the complicated oxidative metabolic pathway for the small-molecule drugs. The results also recommend no correction factors for the scaling of these protein drugs since the SA method produced the lowest average error for human CL prediction (Table 11.4).

11.2.3 Integration of *In Vitro* Metabolic Clearance into Allometric Scaling

With the recent increase in the availability of human liver tissue, metabolic CL in humans may be estimated by a physiological approach using liver microsome, hepatocytes, expressed liver enzymes, or liver perfusion techniques [1,20–28]. Using the below equation, the hepatic blood CL ($CL_{b,H}$) in humans is calculated based on the intrinsic CL (CL_{int}) determined from an *in vitro* system, the LBF (Q_H), and the free fraction in human blood (fu_b).

TABLE 11.4 Multiexponential Allometric Scaling

	SA		MA		SA + MA		SA + MLP	
Drug Molecule	Small	Macro	Small	Macro	Small	Macro	Small	Macro
N	61	18	61	18	61	18	61	18
Average fold error	4.19	2.06	3.52	2.51	3.05	2.79	3.20	3.13
|Fold error| < 2	10 (34%)	14 (78%)	19 (38%)	11 (61%)	30 (50%)	10 (55%)	32 (71%)	9 (50%)
|Fold error| > 2	19	4	40	7	30	8	13	9

[a] SA = simple allometry, $Y = aW^b$. MA = multiexponential allometry, $\mathrm{CL} = aW^b + \left[\frac{1-1.5b}{1-0.5b}\right] aW^b$ SA + MA = rule of exponent—exponent >0.7, MA; exponent <0.7, SA. SA + MLP = rule of exponent—exponent >0.7, corrected by MLP; exponent <0.7, SA.

$$\mathrm{CL_{b,H}} = \frac{Q_\mathrm{H}\cdot \mathrm{fu_b}\cdot \mathrm{CL_{int}}}{Q_\mathrm{H} + \mathrm{fu_b}\cdot \mathrm{CL_{int}}}$$

The *in vitro* systems (i.e., liver microsome, hepatocytes) possess many major drug-metabolizing enzymes and are thus useful tools for the *in vitro* to *in vivo* extrapolation and the prediction of the hepatic metabolic CL in humans. The details of this methodology are discussed in the chapters titled ***Review of Drug Metabolism in Drug Discovery and Development***, ***In Vitro and In Vivo Models of Drug Metabolism***, and ***Enzyme Kinetics of Drug-Metabolizing Reactions and Drug–Drug Interactions*** of this encyclopedia.

As mentioned previously, if there are significant cross-species differences in drug metabolism, the allometric scaling method may not work well. A modified power equation was proposed by Lave *et al*. in 1997 by integration of the *in vitro* data into the allometric relationship to improve the accuracy of hepatic CL prediction in humans. As listed in the following equation, the *in vivo* CL was normalized by the ratio of $\mathrm{CL_{int}}$ between the corresponding animal species and man, where $\mathrm{CL_{int}}$ is obtained from the *in vitro* experiment using liver microsome or hepatocytes and W is the body weight [29]:

$$\mathrm{CL_{man}} = \mathrm{CL_{animal}} \left(\frac{\mathrm{CL_{int,man}}}{\mathrm{CL_{int,animal}}}\right)\left(\frac{W_\mathrm{man}}{\mathrm{W_{animal}}}\right)^b$$

Comparing to the purely empirical approaches, Lave's method using both *in vitro* and *in vivo* experiment data added a physiological exponent to the conventional allometric scaling and gave an opportunity to integrate some of the complexities as discussed above. Lave successfully applied his method for the prediction of human hepatic metabolic CL for 10 compounds mainly eliminated hepatically [29]. Four small-molecule drugs (antipyrine, mibefradil, propranolol, and theophyline) from Lave's list with an allometry exponent $b > 0.80$ and an overpredicted human CL from SA are summarized in Table 11.5. The results suggest that correction with BRW or $\mathrm{CL_{int}}$ could improve the accuracy of human CL prediction and Lave's approach appears slightly better than the BRW method. The average error of human CL prediction is 4.84-, 1.86-, and 1.61-fold for SA, BRW, or $\mathrm{CL_{int}}$ correction, respectively. The scaling plots for propranolol with a comparison of all three methods are presented in Fig. 11.3. Propranolol human CL was nearly 3.5-fold overpredicted using SA (Table 11.5), with a scaling exponent of 0.82. The predicted propranolol human CL was 10.0 and 7.7 mL/min/kg using BRW and $\mathrm{CL_{int}}$ correction, respectively, and both are within twofold of the actual value reported in the literature (13.0 mL/min/kg).

11.2.4 Prediction of Volume of Distribution in Humans

Volume of distribution (V_d) or steady-state volume of distribution (V_dss) in humans is usually well predicted based on animal data. When we use the allometric power equation ($V_\mathrm{d} = aW^b$, $V_\mathrm{dss} = aW^b$) to perform human extrapolation, a plot is normally constructed of total (or unbound) volume of distribution in preclinical species (in units of liter or milliliter) versus animal body weight on a log–log scale for a test compound (Fig. 11.4). Linear regression is performed to determine the values of a and b, and these are then used, along with a standard value for human body weight (e.g., 70 kg), to predict the volume of distribution in humans. As mentioned previously, the allometric exponents for most drugs are in the range of 0.8–1.0 for the scaling of volume of

TABLE 11.5 Human CL Prediction for Antipyrine, Mibefradil, Propranolol, and Theophylline with Simple Allometry (SA), *In vitro* Metabolic Clearance (W_h), or Brain Weight (BRW) Correction

Drug	Exponent b from SA Scaling	Human CL (mL/min/kg)				Predicted/Actual		
		Actual	SA	CL × BRW	CL × W_h	SA	CL × BRW	CL × W_h
Antipyrine	0.93	0.46	5.3	1.2	0.25	11.5	2.6	0.54
Mibefradil	0.90	7.0	42.0	6.3	3.8	6.0	0.90	0.54
Propranolol	0.82	13.0	45.0	7.7	10.0	3.5	0.59	0.77
Theophylline	0.92	0.61	1.4	0.25	0.93	2.3	0.41	1.52
Average fold error						4.8	1.9	1.6

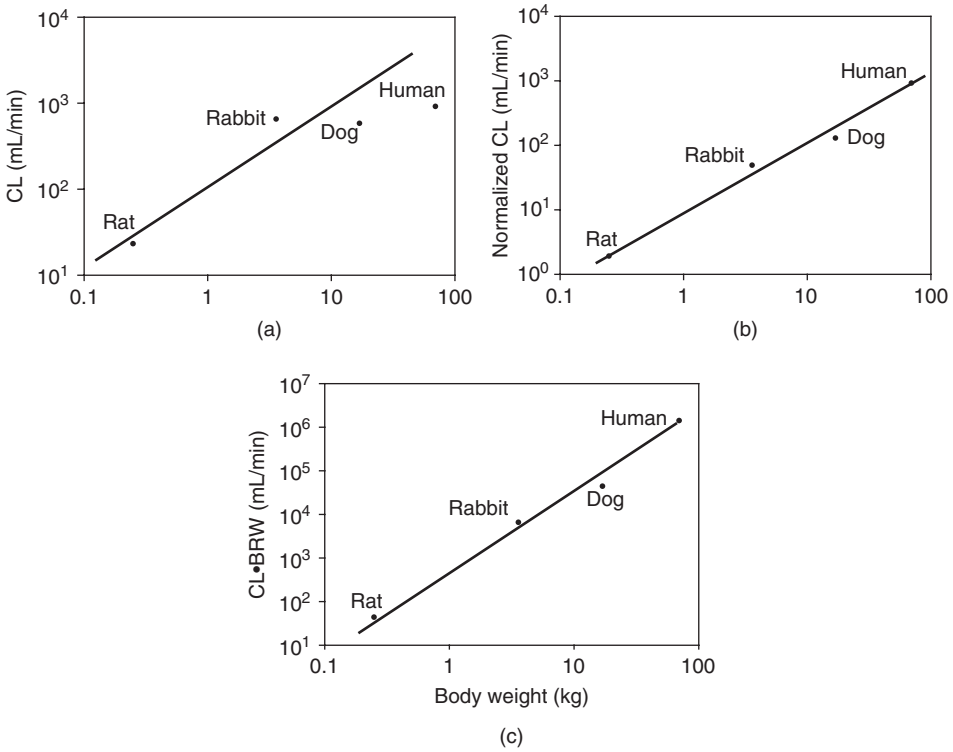

Figure 11.3 Prediction of propranolol human CL with (a) SA (no correction), (b) correction using *in vitro* CL_{int} (normalized CL), and (c) brain weight ($CL \cdot BRW$).

distribution, similar to those from the corresponding biological processes. Boxenbaum in 1982 presented a close relationship ($V_d = 0.756 \cdot W^{0.961}$) between antipyrine volume of distribution and body weight in 11 species including human. His results indicated that the volume of distribution in humans could be successfully predicted using SA [3]. Research from Feng *et al*. [5–7] and other groups [14,31] also support the scaling of V_d or V_{dss} using allometry exponents of 0.8–1.0 with examples presented in Table 11.6 and Fig. 11.4. For the majority of the compounds, the steady-state volume of distribution (V_{dss}) in humans could be estimated using SA with the predicted values within twofold of the actual one (Table 11.6). Although the prediction of diazepam did not work well with the allometric analysis, the error was reduced to twofold when another method using the "average fraction unbound in tissues" was applied, and the details of this method are discussed below.

Obach *et al*. [31] have reported several methods for the prediction of volume of distribution in 1997. In addition to the SA, they also evaluated the contribution of protein binding, and the potential of using the dog–human proportionality or the average fraction unbound in tissues for human extrapolation. The dog–human proportionality method is developed based on the assumption that tissue binding of drugs is similar in dogs and humans, and the physiological parameters, such as extracellular fluid volumes, are similar between the two species on a per-weight basis. Therefore, proportionality could be set up between the free fraction of drug in plasma and the volume

TABLE 11.6 Prediction of Steady-State Volume of Distribution in Humans for 14 Drugs

Drug	Exponent	V_{dss} (L/kg)		
		Predicted (P)	Actual (A)	Ratio (P)/(A)
Cefotetan	0.98	0.21	0.13	1.56
Cefmetazole	0.85	0.15	0.14	1.03
Cefoperazone	0.93	0.17	0.14	1.21
Moxalactam	0.94	0.17	0.14	1.24
Cefpiramide	0.82	0.12	0.11	1.04
Cefazolin	0.98	0.17	0.11	1.60
Erythromycin	0.75	1.33	0.94	1.42
Oleandomycin	0.79	1.30	0.81	1.59
CI-921	0.67	0.29	0.32	0.91
Amsacrine	0.80	1.38	1.56	0.88
SK&F	0.93	0.20	0.24	0.80
Sumatriptan	0.97	2.53	1.64	1.55
Tolcapone	0.94	0.17	0.11	1.47
Diazepam[a]	1.36	7.05	0.89	7.93
Average	0.91	—	—	1.73

[a]Corrected by protein bonding.

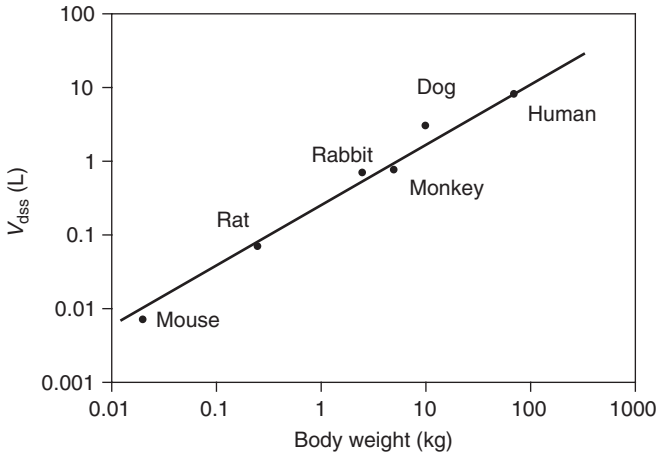

Figure 11.4 Allometric scaling of steady-state volume of distribution (V_{dss}) for cefotetan.

of distribution at steady state in these two species. The equation for the dog–human proportionality method is listed below, where the term "fu" designates the fraction of drug unbound in the plasma (or serum) in dog or human, and V_{dss} (human) and V_{dss} (dog) represent the volume of distribution at steady state in human (predicted) and in dog (actual), respectively, in units of L/kg.

$$V_{dss(human,predicted)} = \left(\frac{fu_{(human)} \cdot V_{dss(dog)}}{fu_{dog}} \right)$$

For the method named as *average fraction unbound in tissues*, experimentally determined values for volume of distribution (in units of L/kg) and unbound fraction in plasma (fu) for each species were used, along with standard values for extracellular fluid volumes, plasma volumes etc., to calculate the fraction unbound in tissues (fu_t) in animal species [43]. After fu_t was calculated for each of the preclinical species, all values for a given compound were averaged. This averaged animal value for *fut* is assumed to be equal to the *fut* in humans and, along with the experimentally determined fu value for humans, was used in the prediction of human V_{dss}.

As listed in Table 11.7, the average error of human V_{dss} prediction was 1.6-, 1.6-, 1.8-, and 2.8-fold for the methods of "dog–human proportionality," "average fraction unbound in tissues," "SA with correction for fu," and "SA without correction for fu," respectively. On the basis of the results, Obach *et al*. recommended using the "dog–human proportionality" or the "average fraction unbound in tissues" method for the prediction of human V_{dss} in drug discovery and development.

As summarized in Fig. 11.5, early projection of CL and volume of distribution in humans is of great significance during drug discovery to assist in the optimization of drug PK characteristics. CL, when combined with the volume of distribution, gives the estimation of elimination half-life ($t_{1/2}$) of a drug. Hepatic metabolic CL, when combined with the fraction absorbed, determines the oral bioavailability ($\%F$) of a drug. Half-life and the oral bioavailability are key determinants of the dosing regimen of oral drugs, that is, size of dose and frequency of administration. Thus, the accurate prediction of CL and volume of distribution in humans is critical in the selection of

TABLE 11.7 Comparison of Various Methods Used for the Prediction of Steady-State Volume of Distribution in Humans

Method	*N*	Average Fold Error
Average fraction unbound in tissues	16	1.56
Dog–human proportionality	16	1.56
SA without correction of free fraction in plasma	14	2.78
SA with correction of free fraction in plasma	12	1.83

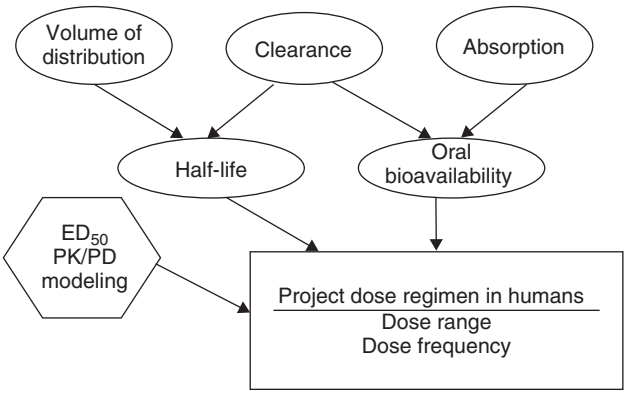

Figure 11.5 Projection of dosing regimen in humans.

new lead compounds for progression into development, as new drugs on the market must not only be efficacious and safe but also be convenient to use for patients and physicians.

11.2.5 Prediction of Pharmacokinetic Profiles in Humans with Nonlinear Mixed Effects Modeling

The use of a nonlinear mixed effects model (NONMEM) as a single-step approach for interspecies scaling has offered certain advantages. This approach could estimate all the allometric parameters in one step and assess interindividual variability in the population. The PK parameters (e.g., CL or volume of distribution) for each species (including human) will then be calculated based on the body weight. The NONMEM equations often used for a two-compartment PK modeling following a single intravenous dose are listed below:

$$\begin{aligned}
\mathrm{TV}V_1 &= \theta_1(W)^{\theta_5} \\
\mathrm{TV}V_2 &= \theta_2(W)^{\theta_6} \\
\mathrm{TVCL} &= \theta_3(W)^{\theta_7} \\
\mathrm{TV}Q &= \theta_4(W)^{\theta_8} \\
V_1 &= \mathrm{TV}V_1 \cdot \exp(\eta_1) \\
V_2 &= \mathrm{TV}V_2 \cdot \exp(\eta_2) \\
\mathrm{CL} &= \mathrm{TVCL} \cdot \exp(\eta_3) \\
Q &= \mathrm{TV}Q \cdot \exp(\eta_4)
\end{aligned}$$

where TV is the population estimate (or typical value) of the PK parameter; θ represents each of the allometric parameters; W is the body weight; CL represents the systemic CL; V_1 and V_2 are the volume of distribution for the central and the peripheral compartments, respectively; Q is the intercompartment CL; and η is the estimate of interindividual variability for each of the PK parameters.

A population pharmacokinetic model was developed and applied to the interspecies PK scaling of pegylated r-HuEPO (PEG-EPO). With NONMEM, the PK profiles of pegylated r-HuEPO (PEG-EPO) and the associated variability were appropriately described in all species (rat, rabbit, monkey, dog, and human) [44]. Another example is the interspecies PK scaling of sumatriptan using mixed effect modeling. The predicted kinetic parameters in each species were close to the actual values from the literature. The mixed effect modeling approach allowed the assessment of covariates associated with the physiologic status of animal (e.g., pregnancy) in the model, which resulted in an improved accuracy in the estimation of human PK parameters and concentration–time profiles [45].

The authors have assessed the interspecies allometric scaling of SK&F and propranolol using the NONMEM approach and the results are presented in Fig. 11.6 [45–50]. Animal data from rat, monkey, and dog were pooled and analyzed in one step using a mixed effect modeling approach (population), and the predicted PK parameters (CL, volume of distribution, etc.) and the plasma concentration–time profiles in humans are closely correlated with the observed values.

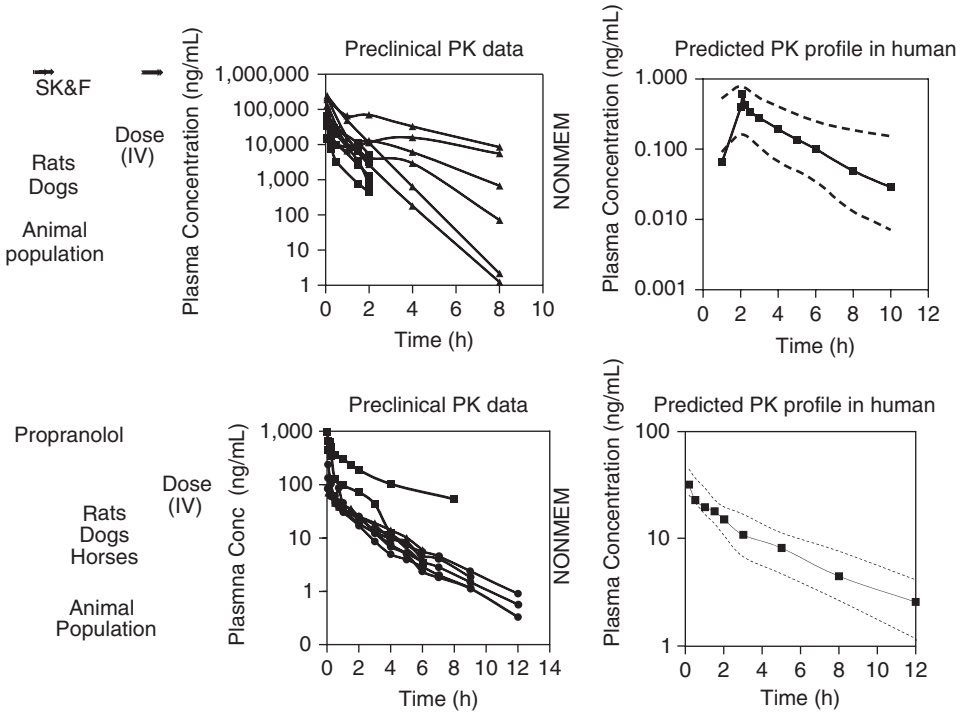

Figure 11.6 Prediction of human PK profiles using nonlinear mixed effects modeling (NONMEM). Symbols used for the preclinical PK plots: square, rat; triangle, dog; and circle, horse. Symbol and line used for the predicted human PK plots: square, observed human PK data and dashed line, upper and lower boundaries of the predicted human PK profile.

Recently, Tabata *et al*. reported a population pharmacokinetic (e-PPK) model for predicting human PK using exploratory ADME (absorption, distribution, metabolism, and excretion) data during early drug discovery research. The model was developed based on data of 11 internal compounds and validated with 12 external compounds. Among the data sets (internal and external references), the predictive performance has shown good consistency [51]. With the NONMEM approach, it is possible to model successfully more complicated allometric equations, to evaluate the potential contribution of physiological variables in the model, and to handle sparse and unbalanced data (quite frequent with animal data). However, allometric scaling using NONMEM is not applicable in all cases. Some of the reasons for failure arise from the differences in enzyme or transporter activities or in metabolic pathways across the species tested.

11.3 PREDICTION OF HUMAN PHARMACOKINETICS USING CELL MODELS

The human body consists of heterogeneous organs that differ in phospholipid contents, organelle densities, and macromolecule distribution patterns. Enhanced distribution to a specific organelle in the target tissue helps to improve the efficacy while undesired accumulation in a subcellular organelle is usually associated with adverse effects

[52–54]. Many of the newly developed drug molecules are inhibitors or stimulators of subcellular enzymes, receptors, or other targets. The subcellular distribution of these drugs in a target tissue is an important determinant of their efficacy or adverse effects. For example, the mechanism of highly active antiretroviral (ARV) therapy through the blockade of different steps of the retrovirus life cycle is now well established. The nucleoside reverse transcriptase inhibitors (NRTIs), integrase inhibitors, and protease inhibitors (PIs) all act on intracellular targets, and the intracellular drug concentrations are closely correlated to the efficacy and toxicity of ARV drugs [55]. The mitochondria and lysosomes are membrane-bound organelles common to virtually all types of eukaryotic cells. Mitochondria-selective accumulation of certain cationic lipophilic drugs accounts for drug retention in target organs as well as a favorable pharmacological profile in preclinical studies. Lysosomal trapping comprises a large portion of total drug uptake of psychotropic drugs, resulting in a more profound drug uptake in lysosome-rich tissues. For therapeutic proteins and monoclonal antibodies, lysosomal degradation is an important elimination pathway following receptor-mediated endocytosis or nonspecific pinocytosis.

The subcellular distribution of a drug molecule may be estimated to some extent by physicochemical properties and unique organellar characteristics (e.g., membrane potential, intraorganellar acidity, bimolecular composition, and organelle density). In recent years, cell-based physiological models have been developed to help enhance our ability to incorporate the subcellular accumulation/degradation of drug molecules into PK and pharmacodynamic (PD) modeling, and this type of modeling is discussed in this section.

11.3.1 Drug Distribution in Lysosomes

Lysosomes (and endosomes) form a complex intracellular recycling system in all nucleated cells, with relatively high abundance in liver, kidney, spleen, and in certain types of cells in the lung [56]. They are characterized by acidic luminal pH (between pH 5 and 6) and a variety of hydrolases (e.g., glucosidases, lipases, proteases, and nucleases) capable of degrading biomolecules and are involved in the normal turnover of organelles [57]. Morphologically, lysosomes and endosomes generally appear as membrane-delimitated spheres but can be elongated tubules in fibroblasts [58] and microphages [59]. The size and number of lysosomes (and endosomes) are maintained by strict regulation of fusion and biogenesis to keep the cellular complement of lysosomes at a relative constant level. Basic amines and weak bases often have a high volume of distribution resulting from their accumulation in the acidic compartments in the cell, usually the lysosomes [60].

Drug-induced lysosomal swelling can be detected in mammalian cells *in vitro* when incubated with high concentration of lysosomotropic compounds, and large swollen vacuoles can often be identified under electron microscopy, laser scanning microscopy, or fluorescent microscopy (Fig. 11.7a–c). Accumulation of lysosomotropic compounds in the lysosomes is also observed *in vivo* in various tissues including liver, kidney, and lung, with the process spanning several weeks [61–63]. There are over 50 marketed pharmaceuticals that induce lysosomal swelling, and they are all weak bases. Several prescribed drugs, amiodarone, azithromycin, chlorpromazine, gentamicin, imipramine, propranolol, and, most notable of all, chloroquine (CQ) are known to cause lysosomal swelling and severe organ impairment in animals and humans [64–66]. CQ, an

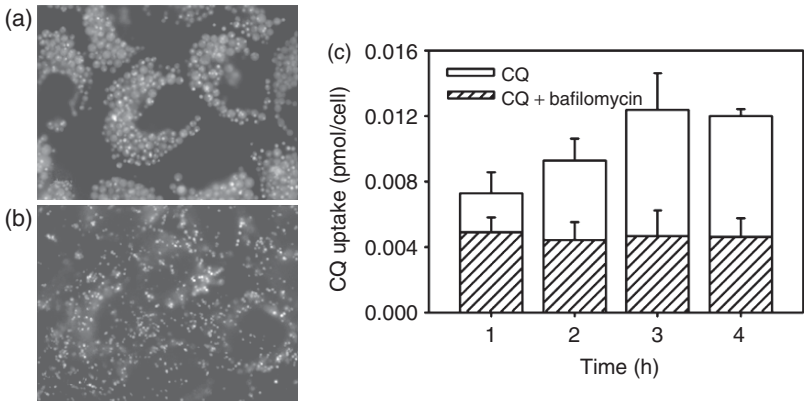

Figure 11.7 Chloroquine (CQ)-induced lysosomal swelling and bafilomycin-inhibited CQ uptake in Madin–Darby canine kidney (MDCK) cells. (a) The swollen lysosomes in cells treated with 50 μM CQ for 4 h, as illustrated by vital staining with 0.5 μM LysoTracker® Green (Molecular Probes, L7526) for 30 min. (b) In cells cotreated with 50 μM CQ and 10 nM bafilomycin A1 for 4 h, lysosomal swelling was inhibited. (c) Intracellular CQ accumulation was inhibited by cotreatment with 10 nM bafilomycin A1.

antimalaria medicine, also known as an *inhibitor of autophagic proteolysis*, inhibits the acidification of lysosomes and endosomes leading to disruption of lysosomal function that impairs maturation of viruses. This mechanism is closely associated with CQ's inhibition effects on human immunodeficiency virus (HIV) and hepatitis C virus (HCV) replication by targeting virus-associated autophagy [67].

A lysosomal trapping model has been developed [68] to describe the dynamic process of lysosomal accumulation induced by basic compounds (Fig. 11.8). In brief, assuming constant pH in the lysosomes and minimum permeability of a protonated molecule, the lysosomal to cytosol concentration ratio (F) of a lysosomotropic compound can be estimated as

$$F = \frac{H_l}{H_e} \quad \text{for monobasic drugs}$$

$$F = \left(\frac{H_l}{H_e}\right)^2 \quad \text{for dibasic drugs}$$

where H_l and H_e are the concentrations of hydrogen ion in the lysosome and the extracellular medium, respectively [56]. Assuming that the intralysosomal pH is 5 and the extracellular pH is 7.2, the F value for a dibasic drug such as CQ ($pK_{a,1} = 10.0$, $pK_{a,2} = 7.5$) can be estimated and appears very high (2.5×10^4). Thus, basic drugs may exhibit a pK_a-dependent accumulation in the lysosomes in cell culture or *in vivo* in lysosome-rich tissues, and this is supported by research from several groups. In an experiment from Orton *et al*. [69], the basic compounds with $pK_a > 8.5$ accumulated extensively in the perfused lung, while amines with $pK_a < 7.0$ showed no sign of accumulation. In a lung perfusion experiment by Anderson *et al*. [70], a pK_a-dependent decrease in replacing amphetamine by other basic drugs was reported. Ishizaki *et al*. [71] discovered a significant reduction of tissue to blood ratio (K_p)

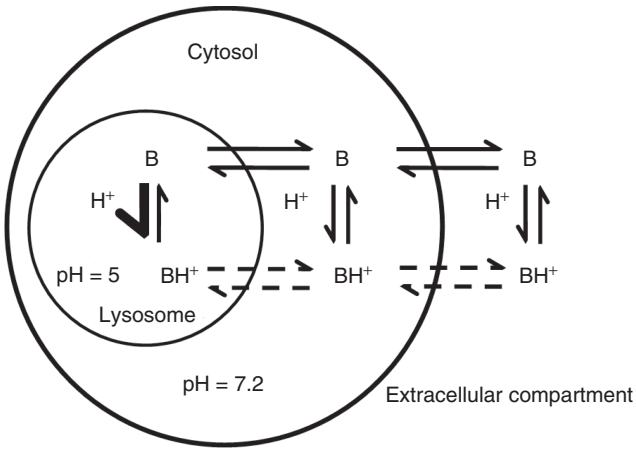

Figure 11.8 Mechanism of lysosomal trapping. Basic drugs in their neutral form may diffuse through the plasma and lysosomal membranes and are then protonated in the acidic lysosomal lumen. These molecules are trapped in the lysosomes due to the poor permeability of the charged form. The lysosomal to extracellular concentration ratio F could be roughly estimated as $F = H_l/H_e$ for a monobasic or $F = (H_l/H_e)^2$ for a dibasic compound, where H_l and H_e are concentrations of hydrogen ion in the lysosome and the extracellular medium, respectively [54,66].

of biperiden and trihexyphenidyl in rat lung, heart, and kidney in the presence of ammonium chloride, a compound that abolishes the pH gradient across lysosomal membranes. They also found a strong positive correlation between lysosomal density and the reduction of K_p caused by ammonium chloride, suggesting an important contribution by lysosomes to the total tissue uptake of both drugs. Similar findings were reported by Hayeshi and collaborators [72] with a significant reduction of intracellular uptake of amodiaquine (a weak base drug) in Caco-2 cells in the presence of the basic compounds CQ and ammonium chloride, both induced an increase of intralysosomal pH.

Lysosomal accumulation significantly affects drug distribution in tissues and organs that contain cells with different lysosomal structures and densities. For example, structural integrity of the lysosomal compartment is required for the uptake of CQ in different tissues [73]. In the mammalian central nervous system, the neuron, astroglia, and oligodendroglia cells form the gray and white matter of the brain. In general, the neuronal cells are highly concentrated in the gray matter, while more glial cells are found in the white matter. Studies in the literature suggested a higher lysosomal density in the neuronal cells (i.e, the gray matter) than in the astroglia and oligodendroglia cells (i.e., the white matter) [74,75]. Daniel *et al*. [76] tested a variety of basic psychotropic drugs and measured the tissue uptake by vertically cut brain slices and cellular uptake by primary neuronal and glial cell cultures. They reported that the steady-state uptake of these psychotropic drugs was more pronounced in the neuronal cells (i.e., gray matter) than in the glial cells (i.e., white matter). In the tissue slices or cell culture experiments, the uptake of these drugs was inhibited by ammonium chloride, a weak base interrupting lysosomal luminal acidity, and the inhibitory effect was more prominent in the neuronal than in the glial cells.

As cited above, basic psychotropic drugs tend to accumulate in the acidic subcellular compartment (i.e., lysosomes), and the accumulation of these drugs in the lysosomes could result in an increase in the intralysosomal pH. A positive correlation was reported between the extent of lysosomal trapping and the therapeutic efficacy of those drugs. In addition, several biochemical processes associated with these pharmacological activities were found altered at enhanced intralysosomal pH [77]. For drugs that function by binding to neurotransmitter receptors and/or transporters, the replacement of a less lysosomotropic compound with a more lysosomotropic psychotropic drug would enhance drug efficacy via distributive interaction with lysosomes [78].

11.3.2 Mitochondrial Sequestration of Drug Molecules

Mitochondria are the energy generators in eukaryotic cells, converting oxygen and nutrients into ATP via aerobic respiration. They appear rod shaped under electron microscopy but form a mobile tubular network *in vivo*. Perhaps, as a result of their prokaryotic origin, mitochondria have two functionally distinct membranes with high lipid and protein composition, as well as an independent genome that codes for a variety of inner membrane proteins [79]. The importance of this organelle is confirmed by an increasing number of diseases associated with the mutation of the mitochondrial genome, malfunction of the respiration pathway, and deregulation of the apoptotic machinery [80–85].

Molecules that exert pharmacological effects via accumulation in the mitochondria or by interaction with mitochondrial proteins represent a structurally diversified group. Among these, lipophilic compounds with delocalized positive charges constitute the largest subgroup with selective mitochondrial accumulation because of the highly negative mitochondrial membrane potential [86]. These molecules can diffuse through lipid bilayers because of their high lipophilicity and are driven into the mitochondrial matrix by the membrane potential gradient [87] (Fig. 11.9). Basic amines can be attracted to mitochondria by the electrical potential and can accumulate in this subcellular organelle; however, the selectivity is relatively low unless specific binding to mitochondrial phospholipids occurs [88–90].

Selective mitochondria-tropic molecules may have applications in anticancer therapy because the mitochondrial membrane potential is notably lower in carcinoma cells than in normal epithelial cells. Therefore, lipophilic cation compounds (mitochondria-tropic) may highly concentrate in carcinoma cells and stimulate an anticancer effect. Chen *et al*. investigated the anticarcinoma activity of two lipophilic cations, dequalinium and MKT-007 [92,93] (Fig. 11.10), and found that both compounds could inhibit the growth of human breast carcinoma cells *in vitro* in a clonogenic assay and prolong the survival rate in mice implanted with tumors. Fluorescent microscope studies further confirmed the selective mitochondrial localization of these two compounds and their toxic effect on mitochondria morphology.

In the field of rational drug design, a series of selective mitochondria-targeted prodrugs have been synthesized by adding a lipophilic cation [e.g., triphenyl phosphonium (TPP)] to the drug molecule (Fig. 11.11) [94–100]. For example, Smith *et al*. [101] covalently attached the TPP cation to the natural antioxidant coenzyme Q to form a prodrug. After oral administration, this mitochondria-targeted coenzyme Q (MitoQ) was rapidly taken up by tissues that are severely affected by mitochondrial dysfunction (the heart, liver, brain, and skeletal muscle), reaching a very high (several hundredfold

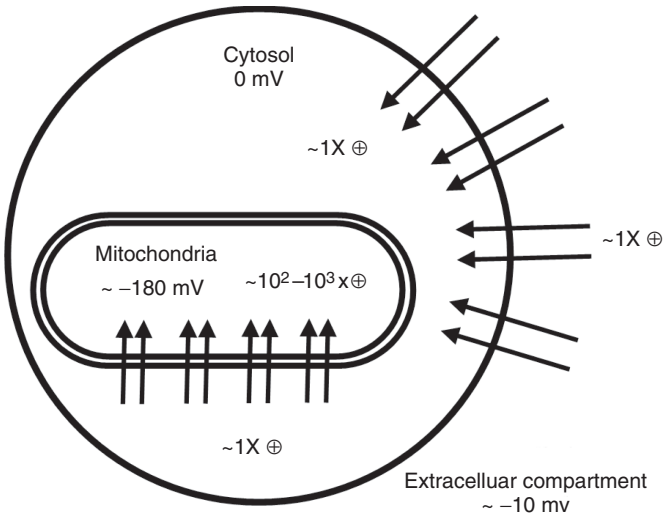

Figure 11.9 Mechanism of mitochondrial selectivity. Driven by electropotential across the membrane, a lipophilic cationic molecule will cross the phospholipid bilayers toward the negatively charged mitochondria lumen. The extent of accumulation can be described by the Nernst equation: $E_{out} - E_{in} = \frac{RT}{zF} \ln \frac{[ion]_{in}}{[ion]_{out}}$, where E is the membrane potential in volt, R is the universal gas constant, T is the absolute temperature, z is the number of positive charge of the ion, F is the Faraday constant, and [ion] is the concentration of the ion. Assuming a negative mitochondrial membrane potential of 180 mV at 37°C [91] and a negative plasma membrane potential of 10 mV compared to the cytosol, a positively charged mono-ion may accumulate in the mitochondria with a concentration approximately10^2- to 10^3-fold higher than that in the extracellular environment [89,90].

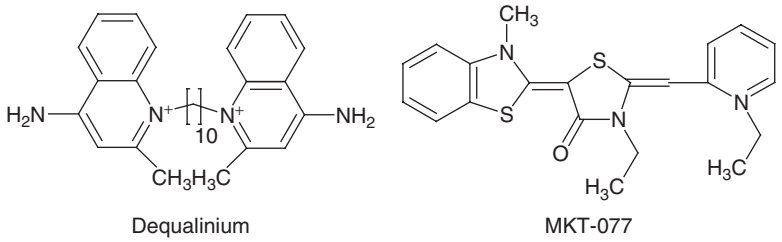

Dequalinium MKT-077

Figure 11.10 Two representative mitochondria-selective lipophilic compounds with delocalized charge(s).

higher) concentration in the mitochondria of these tissues. Meanwhile, the MitoQ was timely cleared from other tissues in the body, leaving no systemic adverse effects. It was also reported that the MitoQ prodrug protected rats from heart dysfunction and cell death caused by ischemia-reperfusion [102], decreased inflammatory response in a rat model with sepsis [103], maintained mitochondrial membrane potential against fluoroquinolone-induced oxidative stress [104], and reduced systolic blood pressure and cardiac hypertrophy in stroke-prone spontaneously hypertensive rats [105]. The synthesis and characteristics of TPP-conjugated antioxidants have been reviewed by Smith and Murphy [106,107].

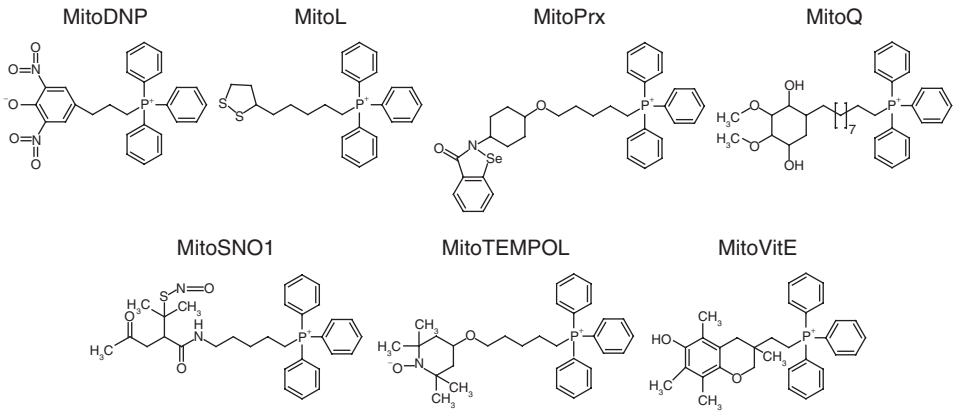

Figure 11.11 Lipophilic molecules with delocalized positive charges targeted to the mitochondria by conjugation to triphenyl phosphonium.

11.3.3 Binding of Drugs to DNA and Other Nonorganelle Components

The cellular composition of proteins, DNA, and phospholipids in plasma, liver, heart, lung, kidney, and many other tissues varies in response to dietary and disease conditions [108]. This could cause high variation in drug–protein (or drug–DNA, drug–phospholipid) interaction in different tissues and affect the disposition, PK, and PD of drug molecules. For example, Nishiura and collaborators [109] revealed that the phosphatidylserine (PhS) content is much higher in the nucleus and membrane fractions than in other organelles in the lung. If a drug molecule preferentially binds to a specific type of lipid component in a subcellular organelle in the tissue, the distribution pattern of this drug may highly correlate with the lipid composition in that organelle. Murata *et al*. [110] reported that the distribution volume of grepafloxacin (GPFX), a quinolone antibacterial agent, is much higher than that of other quinolone antibacterials such as ofloxacin. Suzuki *et al*. have conducted additional studies [111] and identified a positive correlation between the amount of GPFX in subcellular fractions and the PhS content in these fractions (Fig. 11.12). Many anticancer drugs act by interacting with DNA and blocking the biosynthesis of macromolecules. Terasaki *et al*. [112] investigated the tissue distribution of doxorubicin in rats and rabbits and demonstrated a close correlation between tissue uptake of doxorubicin and the levels of DNA in the tissue. Additional studies confirmed the exclusive subcellular localization of doxorubicin associated with the nucleus and a weak correlation between doxorubicin concentration and lipid components. A similar correlation between DNA binding and tissue distribution has also been reported for doxorubicin analogs daunomycin, adriamycinol, daunorubicinol, and actinomycin D [113].

11.3.4 Cell-Based Pharmacokinetic Modeling to Predict the Absorption and Disposition Kinetics in Humans

PBPK models are developed with a series of organ/tissue spaces arranged in a flow diagram incorporating anatomical, physiological, and drug-specific parameters into the model. The whole-body PBPK modeling could help us to predict the kinetic profiles in plasma and in any tissues associated with pharmacological activity or toxicity,

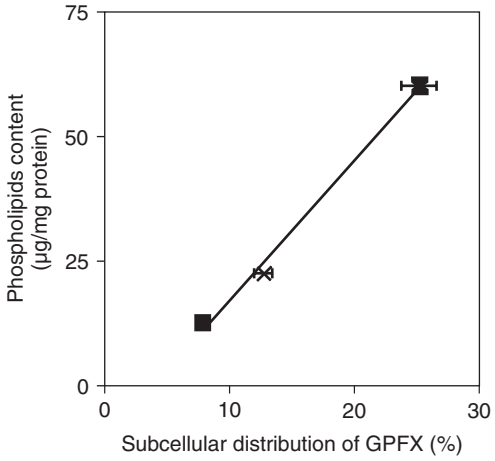

Figure 11.12 Phospholipids composition and subcellular distribution of grepafloxacin (GPFX) in the lung. The contents of phosphatidylserine (PhS) in different subcellular fractions were measured [107] and plotted against the fraction of GPFX discovered in the corresponding subcellular fraction [109]. The majority of GPFX was distributed in the nucleus and plasma membrane fraction (60.3%), followed by the lysosome and mitochondria fraction (22.7%) and the microsome fraction (12.9%). The distribution of GPFX showed good correlation with PhS contents in these subcellular fractions.

and it is a valuable tool to assist the extrapolation of PK/PD information from animals to humans and in decision making in pharmaceutical research and development [114–116]. As discussed previously, the disposition of a drug molecule in the body is controlled by a variety of factors: (i) the organ blood flow and size, (ii) membrane permeability and the physicochemical properties of a drug molecule, and (iii) the binding affinity of the molecule to the plasma/tissue proteins, membrane transporters, and the cytosol/subcellular organelles. Physiologically realistic CBPK models have been developed in recent years to incorporate all these factors in the modeling, and several examples are listed in Tables 11.8 and 11.9. A representative whole-body PBPK model incorporating cell-based mechanism is presented in Fig. 11.13 correlating the cellular events with the disposition of a drug molecule in the body. Single-cell-based pharmacokinetic models were developed in 2005–2008 to simultaneously predict passive transcellular permeability and subcellular distribution of small molecules in polarized epithelial cells [117–119], and one example is presented below. This model consists of several compartments [cellular (cytosol, mitochondria, lysosomes) and extracellular (apical and basolateral)] as described in Equations 11.1–11.4:

$$\frac{dm_c}{dt} = A_a J_{a,c} - A_m J_{c,m} - A_l J_{c,l} - A_b J_{c,b} \tag{11.1}$$

$$\frac{dm_m}{dt} = A_m J_{c,m} \tag{11.2}$$

$$\frac{dm_l}{dt} = A_l J_{c,l} \tag{11.3}$$

$$\frac{dm_b}{dt} = A_b J_{c,b} \tag{11.4}$$

TABLE 11.8 Molecular Characteristics and Drugs with Subcellular Accumulation or Binding

Subcellular Organelles		Distribution	Drugs with Subcellular Accumulation or Binding	Molecular Properties	Mechanisms Involved
Lysosomes		High abundance in liver, kidney, spleen, and some types of cells in the lung [56]	Amiodarone, azithromycin, chlorpromazine, gentamicin, imipramine, propranolol, biperiden, trihexyphenidyl, and chloroquine [62–64]	Weak bases (including some moderate to strong basic compounds)	Ion trapping, electrostatic interactions
Mitochondria		High abundance in muscle	Dequalinium, MKT-007, TPP-conjugated molecules, such as MitoQ [89,90, 92–99]	Lipophilic cations	Passive diffusion, and highly negative mitochondrial membrane potential
Nonorganellar component	DNA	All tissues	Doxorubicin, daunomycin, adriamycinol, daunorubicinol, actinomycin D, [112,113]	Positively charged at physiological pH	Electrostatic interaction
	Lipids	High abundance in adipose [124]	Lipophilic molecules	Lipophilic	Partitioning or electrostatic interaction

TABLE 11.9 Examples of Cell-Based PBPK Models and Application in PK Prediction

Compound	Model Features	References
Napsagatran	Permeability-limited distribution was assumed in the liver; active transport parameters were obtained from *in vitro* hepatocyte experiment, and passive diffusion was negligible based on hepatocyte data; transport proteins involved are still unknown; biliary excretion rate was estimated from bile-duct-cannulated rats.	123
Fexofenadine	Permeability-limited distribution assumed in the liver; active transport parameters were obtained from *in vitro* hepatocyte experiment, and medium passive diffusion was derived from hepatocyte data; it is a substrate of Oatp1a1 and 1a4 (hepatic uptake), Mrp3 (hepatic efflux), Mdr1 and Abcc11 (biliary excretion); biliary excretion rate was estimated from bile-duct-cannulated rats.	123
A variety of bases, acids, neutrals, and zwitterions	Passive diffusion and steady state were assumed; binding to plasma protein, partitioning between neutral and ionic species and neutral lipid, neutral phospholipids, and acidic phospholipids were considered in all major tissues.	124,125
A variety of monovalent molecules	Passive diffusion was assumed; Fick's First Law and Nernst–Planck equation were applied to model the transport of neutral and ionic species across biomembrane. Subcellular accumulation and transcellular permeability of small molecules can be calculated.	117,118
Pravastatin	Active transport with organic anion-transporting polypeptide (OATP) 1B1 and multidrug-resistance-associated protein (MRP) 2 included	126
Methotrexate	Model features permeability-limited compartment for bone marrow, GI tract, spleen, liver, kidney, muscle, and skin; extracellular and intracellular binding were included for those tissues. Permeability-limited tumor compartment was included in a later model.	127,128
SDZ IMM 125	Cell-based PBPK model with three major components: (i) vascular blood cells, (ii) combined interstitial and tissue plasma space, and (iii) tissue cells (rapidly interacting pool and moderately interacting pool).	129
Cyclosporine A	Model features nonlinear intracellular binding and tissue distribution.	130,131
Terbinafine	Cell-based PBPK model with permeability-limited distribution in skin and testis.	132
Fingolimod (FTY720)	Cell-based PBPK model with permeability-limited distribution in brain, thymus, and lymph nodes.	133

Everolimus (RAD001)		Cell-based PBPK model with nonlinear partitioning into red blood cells, nonlinear tissue binding, and degradation in plasma.	120
ISIS 1082		Cell-based PBPK model with permeability-limited distribution in tissues.	134
Domperidone		P-gp-mediated efflux was explored in mouse brain and heart.	135
β−Endorphin		Cell-based PBPK model with capillary-membrane-limited distribution in lung, heart, muscle, skin, liver, gut, kidney, brain, and adipose.	136
Monoclonal antibodies	Monoclonal IgG1	Cell-based PBPK model with lymph circulation. Two-pore model was employed for capillary-membrane-limited step. Binding components were added and specified for different mAbs.	91,137
	BFAs		138
	FcRn		139
	scFv-Fc		140
	Panacarcinoma mAb CC49		121

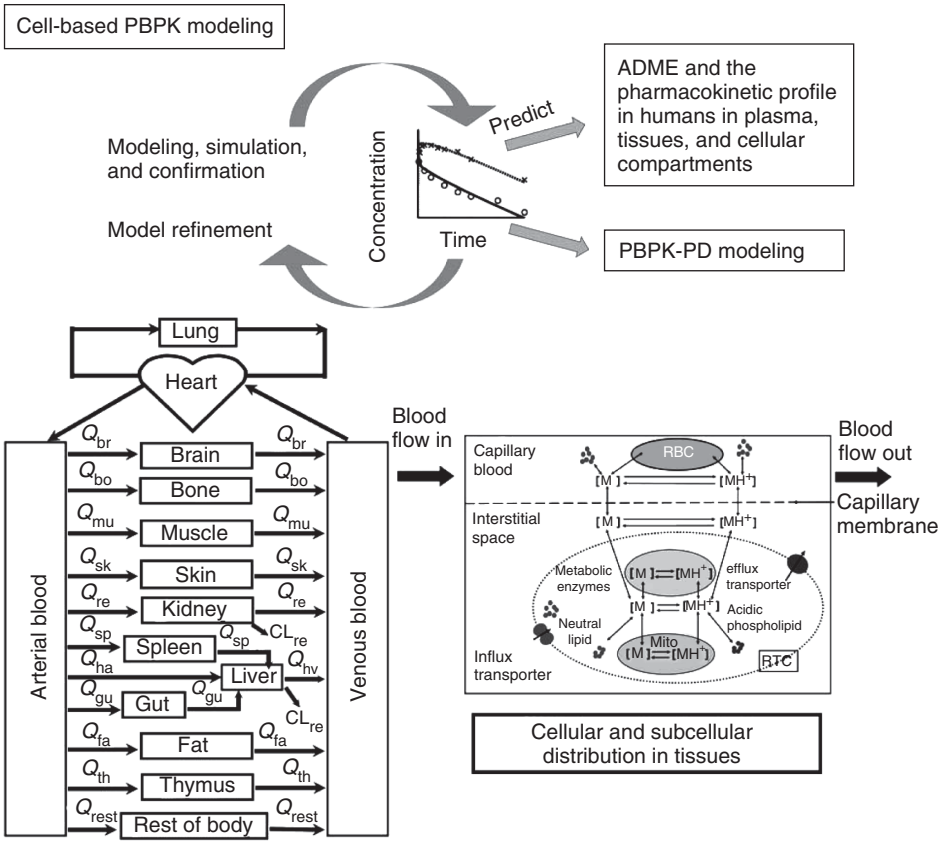

Figure 11.13 Cell-based PBPK modeling and application to human PK/PD prediction. The anatomical/physiological [e.g., size and blood flow (Q) for each tissue] and drug-specific parameters (e.g., ionization, lipophilicity, number of hydrogen bonds, molecular size, polar surface area, red blood cell partitioning, binding to proteins, DNA, and other subcelluar components) are incorporated into the model. RBC, red blood cell; Lyso, lysosome; Mito, mitochondria; RTC, representative tissue cell.

where J is the net flux, m is the total molecular mass, t is time, A is membrane surface area, and the subscripts c, m, l, a, and b represent the cytosol, mitochondria, lysosomes, and extracellular (apical and basolateral), respectively. The concentration in the apical (donor) is assumed to be constant, and the concentration in the basolateral (receiver) compartment is kept at sink condition. The passive diffusion of neutral molecules across the membranes is described by Fick's First Law along the concentration gradient (C_o or C_i) as listed in Equation (11.5):

$$J = P_m(C_o - C_i) \tag{11.5}$$

where P_m is the permeability of the molecules across the cellular membrane.

For electrolytes, the driving force across cellular membrane may be the differences in electrochemical gradient (described by the Nernst–Planck equation). Assuming transmembrane electrical potential to be constant along the membrane, the flux of an ionic

molecule across the membrane is expressed by Equation (11.6);

$$J = -D\left[\frac{\mathrm{d}C(x)}{\mathrm{d}x} + C(x)\left(\frac{zF}{RT}\right)\left(\frac{E}{d}\right)\right] \tag{11.6}$$

where D is the diffusion coefficient (area per time unit); F, R, T, and z are the Faraday constant, molar gas constant, temperature (in Kelvin), and electric charge, respectively; E and d are the membrane potential and thickness, respectively; and $C(x)$ is the concentration of the drug molecule. Equation (11.7) is then derived by integrating Equation (11.6) from 0 to d for x,

$$J = P\frac{N}{\mathrm{e}^N - 1}(C_\mathrm{o} - C_\mathrm{i}\mathrm{e}^N) \tag{11.7}$$

where $P = D/d$ (diffusion coefficient/membrane thickness) and $N = zEF/RT$.

Several other CBPK models have been developed to include subcellular binding (e.g., the binding to tubulins/microtubules) [141–143], the efflux and uptake membrane transporters [e.g., P-glycoproteins (P-gps)], and the hepatic metabolic CL as listed in Table 11.9. For example, paclitaxel's cytotoxicity is closely related to its binding to subcellular tubulins, and a CBPK model was developed based on experiments using human breast MCF7 tumor cells with negligible P-gp expression and human breast carcinoma BC19 cells derived from *mdr1* (i.e., P-gp) transfected MCF7 cells [142]. The outcome from the model analysis indicates that the P-gp-mediated drug efflux accounts for more than 70% of total drug efflux when the extracellular drug concentrations are lower than 200 nM, but the efflux accounts for less than 30% of total efflux when the extracellular drug concentration is 1000 nM. These findings suggest that if patients have P-gp expression in the tumor similar to those in the BC19 cells, the effect of P-gp-mediated drug efflux may not be significant since clinically relevant concentrations are generally higher than 200 nM.

Poirier *et al*. [144] reported a mechanism-based model including active uptake [e.g., via organic anion-transporting peptide (OATP)], nonspecific binding, and saturable hepatic metabolism. Compared to the conventional two-step approach, the CBPK model greatly improved the estimation accuracy and precision of hepatic metabolic CL.

The elimination of pravastatin is mediated by OATP and the multidrug-resistance-associated protein 2 (MRP2), while the pharmacological activities and the side effects are associated with the hepatic disposition kinetics and/or nonspecific accumulation in the muscle and brain tissues. A perfusion limited cell-based PBPK model was developed by Watanabe *et al*. to predict the exposure of pravastatin in plasma, liver, muscle, and brain by integrating data from both *in vitro* and *in vivo* experiments into the model (e.g., active uptake by multiple transporters, hepatic metabolic CL, active biliary excretion) [126]. The liver was segmented into five subcomponents, each consisting of extracellular and hepatocyte compartments. Overall, the cell-based PBPK model gave reasonable predictions, and the model-predicted kinetic profiles of pravastatin in the plasma and tissues were highly correlated with the observed values in rats and humans [126].

In summary, many important biological events at the cellular levels may affect the disposition of drug molecules in the organ/tissue and the whole body. CBPK models may be linked to whole-body PBPK models to predict the effects of cellular events on drug absorption and disposition.

11.4 CONCLUSIONS AND FUTURE PERSPECTIVES

The ability to predict the PK properties (i.e., CL, volume of distribution, elimination half-life, bioavailability, concentration–time profile) during early discovery and development is of great significance for both small-molecule and protein drugs. The interspecies scaling based on animal data and the allometric relationship between body size and biological function is a useful tool widely used in the pharmaceutical industry for this type of projection. The SA method has been successfully applied to the estimation of human CL and volume of distribution for many small- and macromolecule drugs. However, for small-molecule drugs with complicated oxidative metabolic pathway and significant cross-species differences in hepatic metabolism, the SA power equation may not work well for the estimation of human CL, and correction factors (e.g., MLP, BRW, LBF, *in vitro* metabolic CL, free fraction in blood, binding affinity to receptors or subcellular components) have been proposed to enhance the accuracy of prediction. Each of these techniques mentioned above has its own merits and drawbacks, and some of them have had only partial success in predicting human CL. Research work using *in vitro*, *in vivo*, and *in silico* models are still ongoing to further improve the estimation accuracy of human PK profiles to help reduce the risk and the tremendous financial costs associated with failed clinical trials. Cross-species differences in plasma protein binding is another potential problem in interspecies scaling because only the unbound drug molecules are filtered and secreted in the kidney or metabolized and eliminated in the liver. Literature published in this area has demonstrated that human CL would be more accurately predicted using unbound plasma CL. However, accurate measurement of the free fraction (fu) in plasma or blood is critical especially for drugs highly bound to plasma proteins. Experimental error in fu estimation could compromise the scaling results.

Recent advances in computational chemistry have provided additional tools (i) to calculate molecular descriptors (e.g., Log P, Log D, polar surface area and other polar descriptors, free rotatable bonds, atomic charge or free energy associated parameters) to help improve the projection accuracy of the absorption, elimination, and target tissue distribution of drug molecules in humans and (ii) to facilitate the development of cell-based PK/PD models to identify the mechanism associated with biological membrane penetration and drug-receptor/enzyme interaction. For example, high correlation has been reported between the polar surface area (PSA) of a drug molecule and the fraction absorbed in humans [145], or between the PSA and the distribution to brain tissue [146]. Biological mechanism-based models (e.g., PBPK or CBPK models) allow separation of biological and compound-specific components and are thus, by design, capable of integrating information from various processes. By using measurable physiological, anatomical, and biochemical parameters (e.g., organ volume, blood flow rate, binding affinity, and biomembrane permeability), the PBPK or CBPK models can successfully predict the concentration–time profiles in the blood and tissues associated with safety or efficacy in humans [120,121,134,122,147]. The power and utility of PBPK or CBPK models is further increased when linked with mechanistically based PD models [138,148,139,149]. This effective combination is shifting the endpoint of modeling/simulation from a concentration versus time curve toward the time course of a PD outcome. Use of such models can have a major impact during all phases of drug discovery and development and may ultimately result in significant cost reductions for the pharmaceutical industry. In addition, mechanistically based models are

valuable tools for hypothesis testing and mechanistic understanding of the compound's properties and could provide an opportunity to make uncertainty and variability more transparent. With the availability of these models at the preclinical stage, early estimates of the PK/PD profiles in the relevant target (human) population can be obtained to reduce the uncertainty and to improve decision making at early drug discovery and development. This type of combined PBPK/PD or CBPK/PD assessment could provide critical information on the efficacy and safety of drug candidates *in vivo* and bridge the PK/PD concept established during the preclinical development to clinical phase I–III trials. In summary, additional research and investigation are in progress to help increase our ability in performing interspecies scaling and the projection of PK and PD to humans. We believe that the advantage of these newly developed computational models will gradually be recognized and that they will be widely utilized in early drug discovery and development.

REFERENCES

1. Houston JB, Galetin A. Progress towards prediction of human pharmacokinetic parameters from *in vitro* technologies. Drug Metab Rev 2003;35:393–415.
2. Boxenbaum H. Interspecies scaling, allometry, physiological time, and the ground plan of pharmacokinetics. J Pharmacokinet Biopharm 1982;10:201–227.
3. Boxenbaum H, Ronfeld R. Interspecies pharmacokinetic scaling and the Dedrick plots. Am J Physiol 1983;245:R768–R775.
4. Mordenti J, Chen SA, Moore JA, *et al*. Interspecies scaling of clearance and volume of distribution data for five therapeutic proteins. Pharm Res 1991;8:1351–1359.
5. Feng MR, Rossi DT, Strenkoski C, *et al*. Disposition kinetics of cobalt mesoporphyrin in mouse, rat, monkey and dog. Xenobiotica 1998;28:413–426.
6. Feng MR, Loo J, Wright J. Disposition of the antipsychotic agent CI-1007 in rats, monkeys, dogs, and human cytochrome P450 2D6 extensive metabolizers. Species comparison and allometric scaling. Drug Metab Dispos 1998;26:982–988.
7. Feng MR, Lou X, Brown RR, *et al*. Allometric pharmacokinetic scaling: towards the prediction of human oral pharmacokinetics. Pharm Res 2000;17:410–418.
8. Mahmood I. Interspecies scaling: role of protein binding in the prediction of clearance from animals to humans. J Clin Pharmacol 2000;40:1439–1446.
9. Nagilla R, Ward KW. A comprehensive analysis of the role of correction factors in the allometric predictivity of clearance from rat, dog, and monkey to humans. J Pharm Sci 2004;93:2522–2534.
10. Ward KW, Nagilla R, Jolivette LJ. Comparative evaluation of oral systemic exposure of 56 xenobiotics in rat, dog, monkey and human. Xenobiotica 2005;35:191–210.
11. Evans CA, Jolivette LJ, Nagilla R, *et al*. Extrapolation of preclinical pharmacokinetics and molecular feature analysis of "discovery-like" molecules to predict human pharmacokinetics. Drug Metab Dispos 2006;34:1255–1265.
12. Huh Y, Yu J, Tungol A, *et al*. Prediction of human clearance: comparison of small and macromolecule drugs. American Association of Pharmaceutical Scientists Annual Meeting; New Orleans (LA): 2010.
13. Mahmood I. Allometric issues in drug development. J Pharm Sci 1999;88:1101–1106.
14. Mahmood I. Prediction of clearance, volume of distribution and half-life by allometric scaling and by use of plasma concentrations predicted from pharmacokinetic constants: a comparative study. J Pharm Pharmacol 1999;51:905–910.
15. Mahmood I. Interspecies scaling of renally secreted drugs. Life Sci 1998;63:2365–2371.
16. Mahmood I. Interspecies scaling: predicting volumes, mean residence time and elimination half-life. Some suggestions. J Pharm Pharmacol 1998;50:493–499.

17. Mahmood I, Balian JD. Interspecies scaling: predicting clearance of drugs in humans. Three different approaches. Xenobiotica 1996;26:887–895.
18. Tang H, Hussain A, Leal M, *et al*. Interspecies prediction of human drug clearance based on scaling data from one or two animal species. Drug Metab Dispos 2007;35:1886–1893.
19. Goteti K, Brassil PJ, Good SS, *et al*. Estimation of human drug clearance using multiexponential techniques. J Clin Pharmacol 2008;48:1226–1236.
20. Obach RS. Prediction of human clearance of twenty-nine drugs from hepatic microsomal intrinsic clearance data: an examination of *in vitro* half-life approach and nonspecific binding to microsomes. Drug Metab Dispos 1999;27:1350–1359.
21. Houston JB. Utility of *in vitro* drug metabolism data in predicting *in vivo* metabolic clearance. Biochem Pharmacol 1994;47:1469–1479.
22. Hallifax D, Houston JB. Methodological uncertainty in quantitative prediction of human hepatic clearance from *in vitro* experimental systems. Curr Drug Metab 2009;10:307–321.
23. Obach RS. Nonspecific binding to microsomes: impact on scale-up of *in vitro* intrinsic clearance to hepatic clearance as assessed through examination of warfarin, imipramine, and propranolol. Drug Metab Dispos 1997;25:1359–1369.
24. Ito K, Houston JB. Prediction of human drug clearance from *in vitro* and preclinical data using physiologically based and empirical approaches. Pharm Res 2005;22:103–112.
25. Pelkonen O, Turpeinen M. *In vitro -in vivo* extrapolation of hepatic clearance: biological tools, scaling factors, model assumptions and correct concentrations. Xenobiotica 2007;37:1066–1089.
26. Lin JH. Species similarities and differences in pharmacokinetics. Drug Metab Dispos 1995;23:1008–1021.
27. Lin JH, Lu AY. Role of pharmacokinetics and metabolism in drug discovery and development. Pharmacol Rev 1997;49:403–449.
28. Miners JO, Knights KM, Houston JB, *et al*. *In vitro–in vivo* correlation for drugs and other compounds eliminated by glucuronidation in humans: pitfalls and promises. Biochem Pharmacol 2006;71:1531–1539.
29. Lave T, Dupin S, Schmitt C, *et al*. Integration of *in vitro* data into allometric scaling to predict hepatic metabolic clearance in man: application to 10 extensively metabolized drugs. J Pharm Sci 1997;86:584–590.
30. Robbie G, Chiou WL. Elucidation of human amphotericin B pharmacokinetics: identification of a new potential factor affecting interspecies pharmacokinetic scaling. Pharm Res 1998;15:1630–1636.
31. Obach RS, Baxter JG, Liston TE, *et al*. The prediction of human pharmacokinetic parameters from preclinical and *in vitro* metabolism data. J Pharmacol Exp Ther 1997;283:46–58.
32. Riggs DS. The mathematical approach to physiological problems. Baltimore (MD): Williams and Wilkins; 1963. pp. 295–296.
33. Tang L, Persky AM, Hochhaus G, *et al*. Pharmacokinetic aspects of biotechnology products. J Pharm Sci 2004;93:2184–2204.
34. Mahmood I. Pharmacokinetic allometric scaling of antibodies: application to the first-in-human dose estimation. J Pharm Sci 2009;98:3850–3861.
35. Lin JH. Pharmacokinetics of biotech drugs: peptides, proteins and monoclonal antibodies. Curr Drug Metab 2009;10(7):661–691.
36. Yan X, Mager DE, Krzyzanski W. Selection between michaelis-menten and target-mediated drug disposition pharmacokinetic models. J Pharmacokinet Pharmacodyn 2010;37:25–47.
37. Kato M, Kamiyama H, Okazaki A, *et al*. Mechanism for the nonlinear pharmacokinetics of erythropoietin in rats. J Pharmacol Exp Ther 1997;283:520–527.
38. Dirks NL, Nolting A, Kovar A, *et al*. Population pharmacokinetics of cetuximab in patients with squamous cell carcinoma of the head and neck. J Clin Pharmacol 2008;48:267–278.

39. Samtani MN, Perez-Ruixo JJ, Brown KH, *et al*. Pharmacokinetic and pharmacodynamic modeling of pegylated thrombopoietin mimetic peptide (PEG-TPOm) after single intravenous dose administration in healthy subjects. J Clin Pharmacol 2009;49:336–350.
40. Tokuda Y, Watanabe T, Omuro Y, *et al*. Dose escalation and pharmacokinetic study of a humanized anti-HER2 monoclonal antibody in patients with HER2/neu-overexpressing metastatic breast cancer. Br J Cancer 1999;81:1419–1425.
41. Huh Y, Yu J, Tungol A, *et al*. Prediction of human clearance: comparison of small and macromolecule drugs. 2010 AAPS Annual Meeting; New Orleans: 2010.
42. Huh Y, Smith DE, Feng MR, *et al*. Interspecies scaling and prediction of human clearance: comparison of small- and macromolecule drugs. Xenobiotica 2011;41(11):972–987.
43. Oie S, Tozer TN. Effect of altered plasma protein binding on apparent volume of distribution. J Pharm Sci 1979;68:1203–1205.
44. Jolling K, Perez Ruixo JJ, Hemeryck A, *et al*. Mixed-effects modelling of the interspecies pharmacokinetic scaling of pegylated human erythropoietin. Eur J Pharm Sci 2005;24:465–475.
45. Cosson VF, Fuseau E, Efthymiopoulos C, *et al*. Mixed effect modeling of sumatriptan pharmacokinetics during drug development. I: interspecies allometric scaling. J Pharmacokinet Biopharm 1997;25:149–167.
46. le Coutre P, Kreuzer KA, Pursche S, *et al*. Pharmacokinetics and cellular uptake of imatinib and its main metabolite CGP74588. Cancer Chemother Pharmacol 2004;53:313–323.
47. Neville K, Parise RA, Thompson P, *et al*. Plasma and cerebrospinal fluid pharmacokinetics of imatinib after administration to nonhuman primates. Clin Cancer Res 2004;10:2525–2529.
48. Ishizuka M, Nagai S, Sakamoto KQ, *et al*. Plasma pharmacokinetics and CYP3A12-dependent metabolism of c-kit inhibitor imatinib in dogs. Xenobiotica 2007;37:503–513.
49. Oostendorp RL, Buckle T, Beijnen JH, *et al*. The effect of P-gp (Mdr1a/1b), BCRP (Bcrp1) and P-gp/BCRP inhibitors on the *in vivo* absorption, distribution, metabolism and excretion of imatinib. Invest New Drugs 2009;27:31–40.
50. Brocks DR, Freed MI, Martin DE, *et al*. Interspecies pharmacokinetics of a novel hematoregulatory peptide (SK&F 107647) in rats, dogs, and oncologic patients. Pharm Res 1996;13:794–797.
51. Tabata K, Hamakawa N, Sanoh S, *et al*. Exploratory population pharmacokinetics (e-PPK) analysis for predicting human PK using exploratory ADME data during early drug discovery research. Eur J Drug Metab Pharmacokinet 2009;34:117–128.
52. Rancan F, Wiehe A, Nobel M, *et al*. Influence of substitutions on asymmetric dihydroxychlorins with regard to intracellular uptake, subcellular localization and photosensitization of Jurkat cells. J Photochem Photobiol B 2005;78:17–28.
53. Kang TH, Lee JH, Noh KH, *et al*. Enhancing dendritic cell vaccine potency by combining a BAK/BAX siRNA-mediated antiapoptotic strategy to prolong dendritic cell life with an intracellular strategy to target antigen to lysosomal compartments. Int J Cancer 2007;120:1696–1703.
54. D'Souza GG, Cheng SM, Boddapati SV, *et al*. Nanocarrier-assisted sub-cellular targeting to the site of mitochondria improves the pro-apoptotic activity of paclitaxel. J Drug Target 2008;16:578–585.
55. Bazzoli C, Jullien V, Le Tiec C, *et al*. Intracellular pharmacokinetics of antiretroviral drugs in HIV-infected patients, and their correlation with drug action. Clin Pharmacokinet 2010;49:17–45.
56. MacIntyre AC, Cutler DJ. The potential role of lysosomes in tissue distribution of weak bases. Biopharm Drug Dispos 1988;9:513–526.
57. Safting P. Lysosome. Springer; 2005.
58. Heuser J. Changes in lysosome shape and distribution correlated with changes in cytoplasmic pH. J Cell Biol 1989;108:855–864.

59. Swanson J, Bushnell A, Silverstein SC. Tubular lysosome morphology and distribution within macrophages depend on the integrity of cytoplasmic microtubules. Proc Natl Acad Sci U S A 1987;84:1921–1925.
60. Reasor MJ, Kacew S. Drug-induced phospholipidosis: are there functional consequences. Exp Biol Med (Maywood) 2001;226:825–830.
61. Gum RJ, Hickman D, Fagerland JA, *et al*. Analysis of two matrix metalloproteinase inhibitors and their metabolites for induction of phospholipidosis in rat and human hepatocytes(1). Biochem Pharmacol 2001;62:1661–1673.
62. Kacew S. Cationic amphiphilic drug-induced renal cortical lysosomal phospholipidosis: an *in vivo* comparative study with gentamicin and chlorphentermine. Toxicol Appl Pharmacol 1987;91:469–476.
63. McCloud CM, Beard TL, Kacew S, *et al*. *in vivo* and *in vitro* reversibility of chlorphentermine-induced phospholipidosis in rat alveolar macrophages. Exp Mol Pathol 1995;62:12–21.
64. Wibo M, Poole B. Protein degradation in cultured cells. II. The uptake of chloroquine by rat fibroblasts and the inhibition of cellular protein degradation and cathepsin B1. J Cell Biol 1974;63:430–440.
65. Liang M, Knox FG. Nitric oxide activates PKCalpha and inhibits Na+-K+-ATPase in opossum kidney cells. Am J Physiol 1999;277:F859–F865.
66. Lemieux B, Percival MD, Falgueyret JP. Quantitation of the lysosomotropic character of cationic amphiphilic drugs using the fluorescent basic amine Red DND-99. Anal Biochem 2004;327:247–251.
67. Mizui T, Yamashina S, Tanida I, *et al*. Inhibition of hepatitis C virus replication by chloroquine targeting virus-associated autophagy. J Gastroenterol 2010;45:195–203.
68. de Duve C, de Barsy T, Poole B, *et al*. Commentary Lysosomotropic agents. Biochem Pharmacol 1974;23:2495–2531.
69. Orton TC, Anderson MW, Pickett RD, *et al*. Xenobiotic accumulation and metabolism by isolated perfused rabbit lungs. J Pharmacol Exp Ther 1973;186:482–497.
70. Anderson MW, Orton TC, Pickett RD, *et al*. Accumulation of amines in the isolated perfused rabbit lung. J Pharmacol Exp Ther 1974;189:456–466.
71. Ishizaki J, Yokogawa K, Nakashima E, *et al*. Influence of ammonium chloride on the tissue distribution of anticholinergic drugs in rats. J Pharm Pharmacol 1998;50:761–766.
72. Hayeshi R, Masimirembwa C, Mukanganyama S, *et al*. Lysosomal trapping of amodiaquine: impact on transport across intestinal epithelia models. Biopharm Drug Dispos 2008;29:324–334.
73. Daniel WA, Bickel MH, Honegger UE. The contribution of lysosomal trapping in the uptake of desipramine and chloroquine by different tissues. Pharmacol Toxicol 1995; 77:402–406.
74. Hirsch HE. Localization of arylsulphatase in neurons. J Neurochem 1969;16:1147–1155.
75. Freysz L, Farooqui AA, Adamczewska-Goncerzewicz Z, *et al*. Lysosomal hydrolases in neuronal, astroglial, and olidodendroglial enriched fractions of rabbit and beef brain. J Lipid Res 1979;20:503–508.
76. Daniel WA, Wojcikowski J, Palucha A. Intracellular distribution of psychotropic drugs in the grey and white matter of the brain: the role of lysosomal trapping. Br J Pharmacol 2001;134:807–814.
77. Kornhuber J, Retz W, Riederer P. Slow accumulation of psychotropic substances in the human brain. Relationship to therapeutic latency of neuroleptic and antidepressant drugs. J Neural Transm Suppl 1995;46:315–323.
78. Daniel WA. Mechanisms of cellular distribution of psychotropic drugs. Significance for drug action and interactions. Prog Neuropsychopharmacol Biol Psychiatry 2003;27:65–73.
79. Mullins C. The biogenesis of cellular organelles (Molecular biology intelligence unit). Springer; 2005.

80. Kaplan J. Friedreich's ataxia is a mitochondrial disorder. Proc Natl Acad Sci U S A 1999;96:10948–10949.
81. Nishikawa T, Edelstein D, Du XL, *et al*. Normalizing mitochondrial superoxide production blocks three pathways of hyperglycaemic damage. Nature 2000;404:787–790.
82. Raha S, Robinson BH. Mitochondria, oxygen free radicals, disease and ageing. Trends Biochem Sci 2000;25:502–508.
83. Puccio H, Simon D, Cossee M, *et al*. Mouse models for Friedreich ataxia exhibit cardiomyopathy, sensory nerve defect and Fe-S enzyme deficiency followed by intramitochondrial iron deposits. Nat Genet 2001;27:181–186.
84. Li XJ, Orr AL, Li S. Impaired mitochondrial trafficking in Huntington's disease. Biochim Biophys Acta 2010;1802(1):62–65.
85. Liesa M, Palacin M, Zorzano A. Mitochondrial dynamics in mammalian health and disease. Physiol Rev 2009;89:799–845.
86. Horobin RW, Trapp S, Weissig V. Mitochondriotropics: a review of their mode of action, and their applications for drug and DNA delivery to mammalian mitochondria. J Control Release 2007;121:125–136.
87. Murphy MP. Targeting lipophilic cations to mitochondria. Biochim Biophys Acta 2008;1777:1028–1031.
88. Daum G. Lipids of mitochondria. Biochim Biophys Acta 1985;822:1–42.
89. Miniati M, Paci A, Cocci F, *et al*. Mitochondria act as a reservoir for the basic amine HIPDM in the lung. Eur Respir J 1996;9:2306–2312.
90. Daum G, Vance JE. Import of lipids into mitochondria. Prog Lipid Res 1997;36:103–130.
91. Baxter LT, Zhu H, Mackensen DG, *et al*. Physiologically based pharmacokinetic model for specific and nonspecific monoclonal antibodies and fragments in normal tissues and human tumor xenografts in nude mice. Cancer Res 1994;54:1517–1528.
92. Weiss MJ, Wong JR, Ha CS, *et al*. Dequalinium, a topical antimicrobial agent, displays anticarcinoma activity based on selective mitochondrial accumulation. Proc Natl Acad Sci U S A 1987;84:5444–5448.
93. Koya K, Li Y, Wang H, *et al*. MKT-077, a novel rhodacyanine dye in clinical trials, exhibits anticarcinoma activity in preclinical studies based on selective mitochondrial accumulation. Cancer Res 1996;56:538–543.
94. Kelso GF, Porteous CM, Coulter CV, *et al*. Selective targeting of a redox-active ubiquinone to mitochondria within cells: antioxidant and antiapoptotic properties. J Biol Chem 2001;276:4588–4596.
95. Murphy MP, Echtay KS, Blaikie FH, *et al*. Superoxide activates uncoupling proteins by generating carbon-centered radicals and initiating lipid peroxidation: studies using a mitochondria-targeted spin trap derived from alpha-phenyl-N-tert-butylnitrone. J Biol Chem 2003;278:48534–48545.
96. Asin-Cayuela J, Manas AR, James AM, *et al*. Fine-tuning the hydrophobicity of a mitochondria-targeted antioxidant. FEBS Lett 2004;571:9–16.
97. Filipovska A, Kelso GF, Brown SE, *et al*. Synthesis and characterization of a triphenylphosphonium-conjugated peroxidase mimetic. Insights into the interaction of ebselen with mitochondria. J Biol Chem 2005;280:24113–24126.
98. Blaikie FH, Brown SE, Samuelsson LM, *et al*. Targeting dinitrophenol to mitochondria: limitations to the development of a self-limiting mitochondrial protonophore. Biosci Rep 2006;26:231–243.
99. Brown SE, Ross MF, Sanjuan-Pla A, *et al*. Targeting lipoic acid to mitochondria: synthesis and characterization of a triphenylphosphonium-conjugated alpha-lipoyl derivative. Free Radic Biol Med 2007;42:1766–1780.
100. Prime TA, Blaikie FH, Evans C, *et al*. A mitochondria-targeted S-nitrosothiol modulates respiration, nitrosates thiols, and protects against ischemia-reperfusion injury. Proc Natl Acad Sci U S A 2009;106:10764–10769.

101. Smith RA, Porteous CM, Gane AM, *et al*. Delivery of bioactive molecules to mitochondria *in vivo*. Proc Natl Acad Sci U S A 2003;100:5407–5412.
102. Adlam VJ, Harrison JC, Porteous CM, *et al*. Targeting an antioxidant to mitochondria decreases cardiac ischemia-reperfusion injury. FASEB J 2005;19:1088–1095.
103. Lowes DA, Thottakam BM, Webster NR, *et al*. The mitochondria-targeted antioxidant MitoQ protects against organ damage in a lipopolysaccharide-peptidoglycan model of sepsis. Free Radic Biol Med 2008;45:1559–1565.
104. Lowes DA, Wallace C, Murphy MP, *et al*. The mitochondria targeted antioxidant MitoQ protects against fluoroquinolone-induced oxidative stress and mitochondrial membrane damage in human Achilles tendon cells. Free Radic Res 2009;43:323–328.
105. Graham D, Huynh NN, Hamilton CA, *et al*. Mitochondria-targeted antioxidant MitoQ10 improves endothelial function and attenuates cardiac hypertrophy. Hypertension 2009;54:322–328.
106. Murphy MP, Smith RA. Targeting antioxidants to mitochondria by conjugation to lipophilic cations. Annu Rev Pharmacol Toxicol 2007;47:629–656.
107. Smith RA, Adlam VJ, Blaikie FH, *et al*. Mitochondria-targeted antioxidants in the treatment of disease. Ann N Y Acad Sci 2008;1147:105–111.
108. Yamanaka W, Ostwald R. Lipid composition of heart, kidney and lung in guinea pigs made anemic by dietary cholesterol. J Nutr 1968;95:381–387.
109. Nishiura A, Murakami T, Higashi Y, *et al*. Role of phosphatidylserine in the cellular and subcellular lung distribution of quinidine in rats. Pharm Res 1988;5:209–213.
110. Murata M, Tamai I, Sai Y, *et al*. Carrier-mediated lung distribution of HSR-903, a new quinolone antibacterial agent. J Pharmacol Exp Ther 1999;289:79–84.
111. Suzuki T, Kato Y, Sasabe H, *et al*. Mechanism for the tissue distribution of grepafloxacin, a fluoroquinolone antibiotic, in rats. Drug Metab Dispos 2002;30:1393–1399.
112. Terasaki T, Iga T, Sugiyama Y, *et al*. Pharmacokinetic study on the mechanism of tissue distribution of doxorubicin: interorgan and interspecies variation of tissue-to-plasma partition coefficients in rats, rabbits, and guinea pigs. J Pharm Sci 1984;73:1359–1363.
113. Terasaki T, Iga T, Sugiyama Y, *et al*. Nuclear binding as a determinant of tissue distribution of adriamycin, daunomycin, adriamycinol, daunorubicinol and actinomycin D. J Pharmacobiodyn 1984;7:269–277.
114. De Buck SS, Sinha VK, Fenu LA, *et al*. Prediction of human pharmacokinetics using physiologically based modeling: a retrospective analysis of 26 clinically tested drugs. Drug Metab Dispos 2007;35:1766–1780.
115. Lowe PJ, Hijazi Y, Luttringer O, *et al*. On the anticipation of the human dose in first-in-man trials from preclinical and prior clinical information in early drug development. Xenobiotica 2007;37:1331–1354.
116. Jones HM, Parrott N, Jorga K, *et al*. A novel strategy for physiologically based predictions of human pharmacokinetics. Clin Pharmacokinet 2006;45:511–542.
117. Zhang X, Shedden K, Rosania GR. A cell-based molecular transport simulator for pharmacokinetic prediction and cheminformatic exploration. Mol Pharm 2006;3:704–716.
118. Zhang X, Zheng N, Rosania GR. Simulation-based cheminformatic analysis of organelle-targeted molecules: lysosomotropic monobasic amines. J Comput Aided Mol Des 2008;22:629–645.
119. Trapp S, Horobin RW. A predictive model for the selective accumulation of chemicals in tumor cells. Eur Biophys J 2005;34:959–966.
120. Laplanche R, Meno-Tetang GM, Kawai R. Physiologically based pharmacokinetic (PBPK) modeling of everolimus (RAD001) in rats involving non-linear tissue uptake. J Pharmacokinet Pharmacodyn 2007;34:373–400.
121. Davda JP, Jain M, Batra SK, *et al*. A physiologically based pharmacokinetic (PBPK) model to characterize and predict the disposition of monoclonal antibody CC49 and its single chain Fv constructs. Int Immunopharmacol 2008;8:401–413.

122. Yan L, Sheihk-Bahaei S, Park S, *et al*. Predictions of hepatic disposition properties using a mechanistically realistic, physiologically based model. Drug Metab Dispos 2008;36:759–768.
123. Poirier A, Funk C, Scherrmann JM, *et al*. Mechanistic modeling of hepatic transport from cells to whole body: application to napsagatran and fexofenadine. Mol Pharm 2009;6(6):1716–1733.
124. Rodgers T, Leahy D, Rowland M. Physiologically based pharmacokinetic modeling 1: predicting the tissue distribution of moderate-to-strong bases. J Pharm Sci 2005; 94:1259–1276.
125. Rodgers T, Rowland M. Physiologically based pharmacokinetic modelling 2: predicting the tissue distribution of acids, very weak bases, neutrals and zwitterions. J Pharm Sci 2006;95:1238–1257.
126. Watanabe T, Kusuhara H, Maeda K, *et al*. Physiologically based pharmacokinetic modeling to predict transporter-mediated clearance and distribution of pravastatin in humans. J Pharmacol Exp Ther 2009;328:652–662.
127. Lutz RJ, Dedrick RL, Straw JA, *et al*. The kinetics of methotrexate distribution in spontaneous canine lymphosarcoma. J Pharmacokinet Biopharm 1975;3:77–97.
128. Dedrick RL, Zaharko DS, Lutz RJ. Transport and binding of methotrexate *in vivo*. J Pharm Sci 1973;62:882–890.
129. Kawai R, Lemaire M, Steimer JL, *et al*. Physiologically based pharmacokinetic study on a cyclosporin derivative, SDZ IMM 125. J Pharmacokinet Biopharm 1994;22:327–365.
130. Kawai R, Mathew D, Tanaka C, *et al*. Physiologically based pharmacokinetics of cyclosporine A: extension to tissue distribution kinetics in rats and scale-up to human. J Pharmacol Exp Ther 1998;287:457–468.
131. Tanaka C, Kawai R, Rowland M. Physiologically based pharmacokinetics of cyclosporine A: reevaluation of dose-nonlinear kinetics in rats. J Pharmacokinet Biopharm 1999;27:597–623.
132. Hosseini-Yeganeh M, McLachlan AJ. Physiologically based pharmacokinetic model for terbinafine in rats and humans. Antimicrob Agents Chemother 2002;46:2219–2228.
133. Meno-Tetang GM, Li H, Mis S, *et al*. Physiologically based pharmacokinetic modeling of FTY720 (2-amino-2[2-(-4-octylphenyl)ethyl]propane-1,3-diol hydrochloride) in rats after oral and intravenous doses. Drug Metab Dispos 2006;34:1480–1487.
134. Peng B, Andrews J, Nestorov I, *et al*. Tissue distribution and physiologically based pharmacokinetics of antisense phosphorothioate oligonucleotide ISIS 1082 in rat. Antisense Nucleic Acid Drug Dev 2001;11:15–27.
135. Fenneteau F, Turgeon J, Couture L, *et al*. Assessing drug distribution in tissues expressing P-glycoprotein through physiologically based pharmacokinetic modeling: model structure and parameters determination. Theor Biol Med Model 2009;6:2.
136. Sato H, Sugiyama Y, Sawada Y, *et al*. Physiologically based pharmacokinetics of radioiodinated human beta-endorphin in rats. An application of the capillary membrane-limited model. Drug Metab Dispos 1987;15:540–550.
137. Baxter LT, Zhu H, Mackensen DG, *et al*. Biodistribution of monoclonal antibodies: scale-up from mouse to human using a physiologically based pharmacokinetic model. Cancer Res 1995;55:4611–4622.
138. Friedrich SW, Lin SC, Stoll BR, *et al*. Antibody-directed effector cell therapy of tumors: analysis and optimization using a physiologically based pharmacokinetic model. Neoplasia 2002;4:449–463.
139. Ferl GZ, Wu AM, DiStefano JJ. A predictive model of therapeutic monoclonal antibody dynamics and regulation by the neonatal fc receptor (FcRn). Ann Biomed Eng 2005;33:1640–1652.
140. Ferl GZ, Kenanova V, Wu AM, *et al*. A two-tiered physiologically based model for dually labeled single-chain Fv-Fc antibody fragments. Mol Cancer Ther 2006;5:1550–1558.

141. Kuh HJ, Jang SH, Wientjes MG, *et al*. Computational model of intracellular pharmacokinetics of paclitaxel. J Pharmacol Exp Ther 2000;293:761–770.
142. Jang SH, Wientjes MG, Au JL. Kinetics of P-glycoprotein-mediated efflux of paclitaxel. J Pharmacol Exp Ther 2001;298:1236–1242.
143. Jang SH, Wientjes MG, Au JL. Interdependent effect of P-glycoprotein-mediated drug efflux and intracellular drug binding on intracellular paclitaxel pharmacokinetics: application of computational modeling. J Pharmacol Exp Ther 2003;304:773–780.
144. Poirier A, Lave T, Portmann R, *et al*. Design, data analysis, and simulation of *in vitro* drug transport kinetic experiments using a mechanistic *in vitro* model. Drug Metab Dispos 2008;36:2434–2444.
145. Kelder J, Grootenhuis PD, Bayada DM, *et al*. Polar molecular surface as a dominating determinant for oral absorption and brain penetration of drugs. Pharm Res 1999;16:1514–1519.
146. Feng MR. Assessment of blood-brain barrier penetration: in silico, *in vitro* and *in vivo*. Curr Drug Metab 2002;3:647–657.
147. Yu JY, Rosania GR. Cell-based multiscale computational modeling of small molecule absorption and retention in the lungs. Pharm Res 2010;27:457–467.
148. Leger F, Loos WJ, Bugat R, *et al*. Mechanism-based models for topotecan-induced neutropenia. Clin Pharmacol Ther 2004;76:567–578.
149. Ng CM, Patnaik A, Beeram M, *et al*. Mechanism-based pharmacokinetic/pharmacodynamic model for troxacitabine-induced neutropenia in cancer patients. Cancer Chemother Pharmacol 2011;67:985–994.